Global Biogeochemical Cycles

RESEARCH ARTICLE
10.1029/2025GB008499

Surface Water Iron Deposition Histories and the Initiation of Phytoplankton Blooms in the North Pacific Subtropical Gyre

Kyeong Pil Kong[1], Shun-Chung Yang[1], Benedetto Barone[2,3], Douglas S. Hamilton[4], and Seth G. John[1]

[1]Department of Earth Sciences, University of Southern California, Los Angeles, CA, USA, [2]Daniel K. Inouye Center for Microbial Oceanography: Research and Education, University of Hawai'i at Mānoa, Honolulu, HI, USA, [3]Department of Oceanography, University of Hawai'i at Mānoa, Honolulu, HI, USA, [4]Department of Marine, Earth and Atmospheric Sciences, North Carolina State University, Raleigh, NC, USA

Key Points:

- The concentration of iron measured within a phytoplankton bloom was higher than that measured in the absence of a bloom
- Modeling suggests that a wet deposition event delivered a considerable amount of aerosol Fe to the bloom roughly 1 month before its formation
- We developed methods that explore the role of aerosol Fe in stimulating marine phytoplankton productivity

Supporting Information:

Supporting Information may be found in the online version of this article.

Correspondence to:

K. P. Kong,
kyeongpi@usc.edu

Citation:

Kong, K. P., Yang, S.-C., Barone, B., Hamilton, D. S., & John, S. G. (2026). Surface water iron deposition histories and the initiation of phytoplankton blooms in the North Pacific Subtropical Gyre. *Global Biogeochemical Cycles*, *40*, e2025GB008499. https://doi.org/10.1029/2025GB008499

Received 6 JAN 2025
Accepted 22 DEC 2025

Author Contributions:

Conceptualization: Kyeong Pil Kong, Benedetto Barone, Seth G. John
Data curation: Kyeong Pil Kong, Shun-Chung Yang, Benedetto Barone, Douglas S. Hamilton
Formal analysis: Kyeong Pil Kong, Benedetto Barone, Douglas S. Hamilton, Seth G. John
Funding acquisition: Benedetto Barone, Douglas S. Hamilton, Seth G. John
Methodology: Kyeong Pil Kong, Shun-Chung Yang, Benedetto Barone, Seth G. John
Supervision: Seth G. John

Abstract Highly productive summer phytoplankton blooms in the central North Pacific Subtropical Gyre (NPSG) are an annual occurrence that leads to the export of considerable amounts of surface particulate carbon to depth. The mechanisms that control the formation of these blooms remain unresolved, but iron (Fe) availability may be an important factor. From July to October 2022, a large, persistent phytoplankton bloom was detected near 23.3°N, 154.6°W in satellite imagery and in situ measurements. Elevated Fe concentrations and nitrogen (N_2) fixation activity measured within the bloom suggest that high Fe may have supported enhanced diazotrophic activity. To evaluate whether aerosol deposition created favorable conditions for bloom formation, we reconstructed the Fe deposition history of the bloom's source waters by integrating surface water back trajectory analyses with aerosol Fe flux simulations. Our results show that waters that hosted the diatom-diazotroph assemblage bloom received up to 20% more soluble Fe through aerosol deposition than its surrounding waters, primarily from a strong wet deposition event that occurred approximately 1 month before the bloom. The observed lag between deposition and bloom suggests a delayed biological response to atmospheric Fe inputs. Although this moderate increase does not represent incontrovertible evidence that the bloom was stimulated by aerosol Fe deposition, our findings establish the potential for episodic delivery of atmospheric Fe to stimulate diazotrophic activity and phytoplankton growth over month-long timescales in the NPSG.

Plain Language Summary In July 2022, a large phytoplankton bloom formed in the surface ocean northeast of the Hawaiian Islands. Within the bloom, we measured high iron concentrations in waters where high levels of biomass were present. The bloom was enriched in organisms that fix atmospheric nitrogen, an iron intensive process. We observed that a large pulse of atmospheric iron was deposited 4 weeks prior to the formation of the bloom and may have played a role in providing critical nutrients to the waters where nitrogen fixing organisms can rapidly grow. We leveraged models to determine when and how much atmospheric iron was deposited in the surface water where the bloom formed.

1. Introduction

Marine phytoplankton play a critical role in regulating the global carbon cycle, contributing approximately half of the Earth's primary production through carbon fixation (Field et al., 1998). An estimated 20% of this net primary production—equivalent to 5–10 GT C annually—is exported to the deep ocean through the biological pump (Falkowski et al., 1998; Palmer & Totterdell, 2001). Although subtropical gyres in oceans are generally characterized by low biomass and productivity, they contribute to nearly 20% of global ocean net primary productivity and account for 23% of the total ocean carbon dioxide (CO_2) export (Dai et al., 2023; Iida et al., 2021). The North Pacific Subtropical Gyre (NPSG) is an oligotrophic region marked by strong surface stratification and persistently low inorganic nutrient availability in the surface layer (Bathen, 1972; Dave & Lozier, 2010; Karl, 1999). In this system, nitrogen (N_2) fixing microbial organisms (diazotrophs) supply approximately half of the new nitrogen produced on the surface and represent a major source of bioavailable ammonia (Böttjer et al., 2017; Dore et al., 2008; Karl et al., 1997). Since the nitrogenase enzyme used to fix atmospheric N_2 within diazotrophs has a high requirement for iron (Fe), diazotrophy, and by extension, primary productivity, may be suboptimal in Fe limited waters (Falkowski, 1997; Hutchins & Sañudo-Wilhelmy, 2021; Whittaker et al., 2011). At Station A Long-term Oligotrophic Habitat Assessment (ALOHA; 22°45′N, 158°W), N_2 fixation may be sensitive to Fe

Validation: Kyeong Pil Kong, Shun-Chung Yang

and/or phosphorus (P) availability, although the relative importance of these controls remains unresolved (Follett, White, et al., 2018; Grabowski et al., 2008; Letelier et al., 2019).

1.1. The Relationship Between Fe and Nitrogen Fixation

Marine N_2 fixation is generally greater in regions with elevated dust input, likely as a result of the high Fe requirement of diazotrophs. In the North Atlantic, dust input from North Africa supplies substantial Fe in dust aerosols and supports high N_2 fixation rates relative to the South Atlantic (Jickells et al., 2005; Moore et al., 2009). Under such Fe-replete conditions, N_2 fixation by *Trichodesmium* in the North Atlantic is considered P-limited rather than Fe-limited (Webb et al., 2007). As a result, *Trichodesmium* populations in the North Atlantic are one order of magnitude higher than those in the North Pacific and do not express the Fe stress gene *isiB*, which is upregulated by *Trichodesmium* in the North Pacific (Chappell et al., 2012; Sohm, Webb, & Capone, 2011). Other diazotrophs such as unicellular diazotrophic cyanobacteria (UCYN) including *Crocosphaera* are also sensitive to Fe availability (Jacq et al., 2014).

Incubation experiments have been used to determine whether Fe additions can stimulate N_2 fixation activity, but the outcomes have been inconsistent. Grabowski et al. conducted a 24-hr incubation study where seawater obtained from Station ALOHA was amended with nutrient treatments including P and Fe, and found variable results. While the addition of either P or Fe led to an increase in nitrogen fixation activity, the addition of both P and Fe together resulted in a decline in nitrogen fixation activity. Tanita et al. (2021) conducted separate experiments where Fe and P were added to surface waters collected across the Pacific Ocean including waters from the western and central NPSG. After 48 hr, they observed an increase in nitrogen fixation only in waters from the western NPSG. These contrasting results suggest that while Fe availability can influence diazotrophy, the biogeochemical context of the surface waters, including background nutrient levels and microbial community structure, modulates response to new Fe inputs.

1.2. Controls on Nitrogen Fixation and Productivity in the NPSG

In the NPSG where productivity is limited by low new nutrient inputs, rapid recycling of existing material results in low export efficiencies compared to more productive ocean basins (Karl et al., 2021). Despite this nutrient scarcity, summertime phytoplankton blooms in the NPSG occur annually (Villareal et al., 2011; C. Wilson, 2003). These occurrences contribute to the NPSG summer export pulse and can sequester substantial amounts of nitrogen and atmospheric carbon to depth (Dore et al., 2008; Karl et al., 2012; Quay & Stutsman, 2003; Villareal et al., 2011; C. Wilson & Coles, 2005). Within blooms, diazotrophs such as *Trichodesmium* or *Richelia* (symbiotically existing within *Hemiaulus*) are often abundant (Brzezinski et al., 1998; Karl et al., 1992; Mague et al., 1974; Villareal et al., 2011). However, blooms of other N_2 fixers such as *Crocosphaera* have also been observed in this region (S. T. Wilson et al., 2017). Consequently, the formation of summertime blooms in the NPSG is often linked to an increase in N_2 fixation (Böttjer et al., 2017), even though the processes underlying the accumulation of diazotrophs remain unresolved. N_2 fixation activity in the NPSG is thought to be controlled by Fe and P availability among other factors; therefore, an increase in Fe deposition during the spring and summer may lead to an increase in N_2 fixation during the summer (Follett, Dutkiewicz, et al., 2018; Letelier et al., 2019).

Aerosol deposition of Fe from three major sources (lithogenic, biogenic, and anthropogenic) serves as a major input of Fe to the surface of the NPSG (Fitzsimmons et al., 2015). The solubility of these Fe sources (i.e., the fraction of soluble Fe to total Fe) controls their bioavailability to phytoplankton (Baker & Jickells, 2006). While Fe-containing mineral dust comprises a larger portion of the total Fe deposited on the ocean's surface, Fe from anthropogenic combustion and biomass burning is more soluble and thus more bioavailable to the microorganisms (Chuang et al., 2005; Guieu et al., 2005; Ito et al., 2019; Mahowald et al., 2005; Sedwick et al., 2007). With the precipitous increase in fossil fuel combustion in East Asia, pyrogenic and anthropogenic Fe have been playing an increasingly larger role in delivering soluble Fe to the North Pacific in recent decades (Hamilton et al., 2020; Pinedo-González et al., 2020). Models estimate that anthropogenic sources may supply half of atmospheric soluble iron to the North Pacific waters (Rathod et al., 2020, 2024), consistent with recent observations (e.g., Hawco et al., 2025; Zhang et al., 2024). However, aerosol deposition of Fe is inherently episodic as it depends on the emission, atmospheric transport, and deposition of particles; processes that are dependent upon environmental and meteorological conditions that change across space and time (Hamilton et al., 2020; Smith et al., 2017). As a result, while rates of N_2 fixation and the formation of high chlorophyll blooms may be expected in the NPSG from

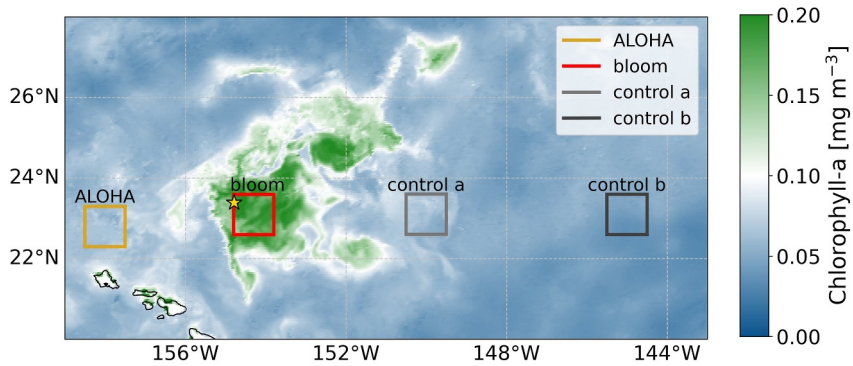

Figure 1. Satellite-derived map of chlorophyll *a* concentration on 7 August 2022 showing the 2022 bloom north of the Hawaiian Islands. Samples from the bloom were collected during the PARAGON-2 expedition (gold star). Initial water parcel locations for the back trajectory analysis within the bloom (red square) and from control locations outside the bloom including Station ALOHA (yellow square), Control A (light gray square), and Control B (dark gray square).

the increase in soluble Fe deposition, the variable nature of aerosol deposition events may make prediction of such phenomena difficult, especially at the weeks-to-months temporal scale of phytoplankton blooms.

Here, we investigate a single bloom event that started in July 2022 henceforth referred to as the 2022 bloom. The 2022 bloom spanned over 220,000 km^2 in aerial extent at its peak in August (Foreman et al., 2025). Seawater analyses of this bloom revealed cell abundances of the diatom *Hemiaulus hauckii* to be an order of magnitude higher compared to cell abundances found in typical non-bloom periods (Anderson et al., 2018; Foreman et al., 2025). *Hemiaulus* represented approximately 40% of the total volume of particles imaged (~4–100 µm diameter size) with the Imaging FlowCytoBot from seawater in the 2022 bloom, inclusive of non-fluorescent detrital material (Foreman et al., 2025). Furthermore, gene copies of *nifH* from *Richelia intercellularis*, an endosymbiotic diazotroph associated with *Hemiaulus*, were also significantly elevated within the 2022 bloom (Foreman et al., 2025). The increased biomass in the 2022 bloom can be predominantly attributed to this diatom-diazotroph assemblage (DDA). Comprehensive details on the hydrographic and biogeochemical characteristics of the 2022 bloom are provided by Foreman et al. (2025).

To explore whether Fe played a pivotal role in stimulating the 2022 bloom, we collected and analyzed seawater within the bloom for trace metal concentrations and the isotopic composition of Fe in the dissolved phase, suspended particulate phase, and sinking particles. In addition, we developed a novel modeling framework that combines surface ocean circulation with aerosol chemistry to reconstruct the deposition history of aerosol Fe onto surface waters. Specifically, we used a model including geostrophic and wind-driven ocean circulation to generate back-trajectories of surface water parcels from the 2022 bloom region as well as from nearby regions where blooms did not occur. These back-trajectories were integrated with a model that quantifies daily aerosol fluxes to determine the timing and magnitude of aerosol Fe delivery to the 2022 bloom. With this work, we aim to better constrain the role of aerosol-derived Fe in driving phytoplankton bloom formation in the NPSG.

2. Materials and Methods

2.1. Sample Collection

Sample collection for this study was conducted aboard *R/V Kilo Moana* as a part of the PARticles And Growth in the Oceanic Nutricline 2 (PARAGON-2) cruise from 4 to 12 August 2022. This expedition targeted an area near the western edge of the 2022 bloom at 23.3°N 154.6°W (Figure 1). Seawater samples for dissolved and suspended particulate trace metal analysis were collected between 25 and 500 m using 8-L external spring loaded Niskin bottles (Ocean Test Equipment) mounted on a powder coated rosette system (Sea-bird Scientific). Seawater for dissolved metals and the isotopic composition of Fe were filtered using acid-cleaned 0.8/0.2 µm Pall Acropak-1000 Supor cartridges into acid-cleaned 1 L low-density polyethylene bottles. Samples were later acidified to pH ~2 by adding 1 mL 12 M distilled hydrochloric acid at the University of Southern California (USC), which were then stored for at least 2 months. Suspended particles from seawater were collected from the same bottles as those collected for filtered seawater by passing water from the Niskin bottles through an in-line filter holder

containing a 25 mm diameter 0.2 μm acid cleaned Supor membrane filter for a maximum of 2 hours (3.3–4.0 L). The filters were then stored in acid-washed airtight vials.

Sinking particles were collected using a free-drifting particle interceptor trap (PIT) array (Knauer et al., 1979) containing one to four trace-metal clean traps. The sediment traps were deployed at 130, 200, 225, 250, 350, 400, 500 m at the western edge of the bloom for 3 days. Before deployment, each trap was filled with approximately 2 L of brine containing 80 g l^{-1} trace metal grade sodium chloride (Sigma Aldrich, CAS 7647-14-5) in the lower portion of the trap and 1.5 L of 0.2 μm filtered trace metal clean seawater in the upper portion of the trap. For traps deployed at 130, 225, and 400 m, four total traps were deployed on the PIT cross: three were uncapped to collect sinking particles at depth and one remained capped during the entire deployment to serve as a control trap. For all other depths, only one uncapped trap was deployed for trace metal analysis. Upon recovery of the array, the PITs were capped and taken to a shipboard trace-metal clean van. The overlying seawater was removed, and the brine samples were passed through an acid-washed 335 μm polyethylene mesh screen to remove large zooplankton. Each sample was then vacuum filtered through an acid washed 47 mm 0.2 μm Supor filter and stored in an acid-washed airtight vial.

2.2. Trace Element Concentration and Flux Measurements

Samples for dissolved metal concentrations were analyzed at USC upon seawater preconcentration using an offline seaFAST-pico (Elemental Scientific Inc.) metal extraction method modified from Lagerström et al. (2013). For each sample, aliquots of 15 mL subsamples were mixed with 50 μL of an isotope spike containing ^{57}Fe, ^{62} Ni, ^{65} Cu, ^{67}Zn, ^{207}Pb, and ^{110}Cd. Metals were extracted with Nobias PA-1 resin and eluted into 1.4 M nitric acid containing 10 ppb In. Metal concentrations were then analyzed by inductively coupled mass spectrometry (ICP-MS) on an 8900 Triple Quadrupole ICP-MS (Agilent Technologies).

Samples collected to measure metal concentrations in suspended particles and metal fluxes in sinking particles were also analyzed at USC. Filters from both fractions were digested with 8 M HNO_3 for 12 hr in perfluoroalkoxy (PFA) vials at 100°C (Noble et al., 2013; Planquette & Sherrell, 2012). This digest method does not solubilize metals associated with crustal material or silica frustules (Ingalls et al., 2004; Planquette & Sherrell, 2012). The filters were then removed from the PFA vials, and the sample was evaporated to dryness. The digest material was then resuspended with 0.1 M HNO_3, and a small aliquot was then further diluted with 1.4 M HNO_3 with 10 ppb In for analysis on the 8900 Triple-Quadrupole ICP-MS. Concentrations of Fe from all samples were validated and corrected using the Neptune Plus MC-ICPMS (Thermo Scientific) following purification of Fe from samples outlined in Section 2.3.

Data for procedural blanks, filter blanks, limits of detection, and control sediment trap data are shown in Table S1 in Supporting Information S1. Average filter blanks were subtracted from all measured values, and average control trap values were subtracted from each trap to account for elemental contributions from the brine used in the trap. The same digest procedure was used to process small quantities of certified reference materials BCR-414 (Joint Research Center) and Arizona Test Dust community reference material to determine the efficacy of the digest procedure (Table S2 in Supporting Information S1).

2.3. Isotopic Measurements of Fe (δ^{56}Fe)

Seawater and seawater particle samples were extracted and purified for Fe isotopic analysis following methods outlined by Conway et al. (2013). A double spike containing ^{57}Fe and ^{58}Fe was added to all samples to achieve a spike-to-sample ratio of 2:1. Metals from the filtered seawater samples for dFe isotopic composition analysis were then extracted using Nobias PA-1 chelating resin, where ∼1 g of Nobias resin was added to the sample and shaken for at least 2 hr on an orbital shaker table. The resin was then filtered from the solution using an acid-washed 5 μm polycarbonate filter (Whatman) and rinsed with ∼60 mL 18.2 MΩ·cm ultrapure water. Metals in the resin were eluted with 2 M HNO_3, where the eluent was then evaporated to dryness on a hot plate overnight, refluxed in 14 N HNO_3 for at least 2 hr, and evaporated to dryness again. The digested material from suspended and sinking particulate concentration analyses was spiked, homogenized, and evaporated to dryness. All dried samples (dissolved, suspended particulate, and sinking particulate) were resuspended in 5 M HCl in preparation for Fe purification.

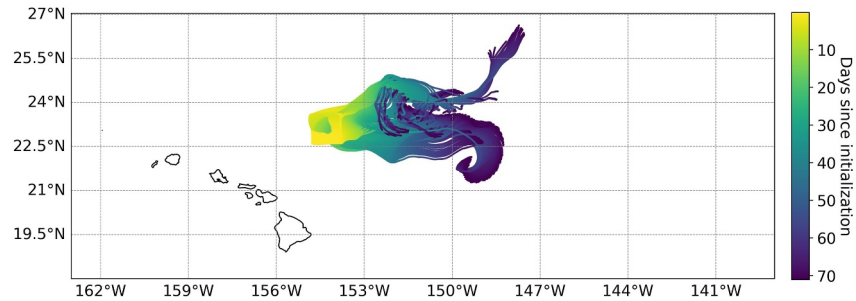

Figure 2. The daily location of back trajectory parcels from the bloom zone from 7 August 2022 to 1 June 2022. Water parcels were initiated within 1° by 1° area (22.5°–23.5°N, 153.6°–154.6°W). Parcels show a westward movement in forward time.

Samples for dissolved and particulate Fe (dFe, pFe, respectively) isotopic analysis were purified using anion exchange chromatography with the AG-MP1 resin (Bio-Rad) in micro-columns (Conway et al., 2013). Fe was eluted using 1 M HCl, evaporated to dryness, and resuspended with 0.1 M HNO_3 with variable volume to achieve 100 ppb Fe of the sample in the solution. The isotopic composition of Fe was then measured on a Neptune Plus MC-ICPMS at USC. Samples were introduced using a PFA nebulizer with a flow rate of 100–120 μL min^{-1} and the Apex 2Q desolvation system. The high-resolution mode was used to resolve possible polyatomic interferences, such as $^{40}Ar^{16}O$, $^{40}Ar^{14}N$, and $^{40}Ar^{18}O$. Four Fe isotopes (^{54}Fe, ^{56}Fe, ^{57}Fe, and ^{58}Fe) were analyzed and ^{52}Cr and ^{60}Ni were monitored simultaneously to correct for any interferences of ^{54}Cr on ^{54}Fe and ^{58}Ni on ^{58}Fe, respectively.

The double spike technique was used to correct for instrumental mass bias and potential Fe isotope fractionation during sample purification. The data reduction scheme followed the iterative method described by Siebert et al. (2001). The Fe isotope ratios were expressed using the conventional delta notation relative to the IRMM-014 Fe isotope standard:

$$\delta^{56}\mathrm{Fe} = \left[\left(^{56}\mathrm{Fe}/^{54}\mathrm{Fe}\right)_{\mathrm{sample}}/\left(^{56}\mathrm{Fe}/^{54}\mathrm{Fe}\right)_{\text{IRMM-014}} - 1\right] \times 1{,}000$$

The external long-term analytical uncertainty of $\delta^{56}Fe$ is ±0.07‰, based on repeated analysis of the secondary Fe isotope standard SRM NIST 3126 (+0.35‰ ± 0.07‰, 2SD, $n = 150$) over the last 4 years. The internal precision of single sample measurement ranged from ±0.02‰ to ±0.15‰, which was obtained by combining the internal precision of both sample and standard measurements (Conway et al., 2013). The analytical reproducibility for the reported $\delta^{56}Fe$ of each sample is the long-term reproducibility, unless the internal uncertainty is larger, in which case the latter is reported.

2.4. Modeled Soluble Fe Deposition Rates and Water Parcel Back Trajectories

Water parcel back trajectories were performed by advecting virtual Lagrangian water parcels from the bloom location and three control locations starting from 7 August 2022 (the day of shipborne sample collection). The back trajectory simulations used satellite derived ocean current from the Ocean Surface Current Analysis Real-time that accounts for both geostrophic currents and wind-driven currents (Bonjean & Lagerloef, 2002). The original data product was provided at a horizontal resolution of 0.25° in latitude and longitude. To improve the algorithm performance near land, the currents were re-interpolated on a finer grid of 0.0625° using a spline algorithm and 0 velocity was assigned to the grid points falling on land masses before interpolation. Water parcel tracking was performed by modifying the MATLAB code provided in the LCS tool (Onu et al., 2015). The maximum temporal resolution was forced not to exceed 0.1 days and currents were calculated using a linear interpolator on the original grid. The trajectories that ended on land were flagged and not used in the statistics (less than 1% for all simulations). Back trajectories of at least 900 virtual water parcels were conducted during each simulation. The back trajectory analysis showed that most parcels in generally moved westward over time (Figure 2, Figure S1 in Supporting Information S1).

Soluble and total Fe aerosol deposition rates were simulated using the Mechanism of Intermediate complexity for Modeling Iron (MIMI) model within the Community Earth System Model (CESM), as described by Hamilton

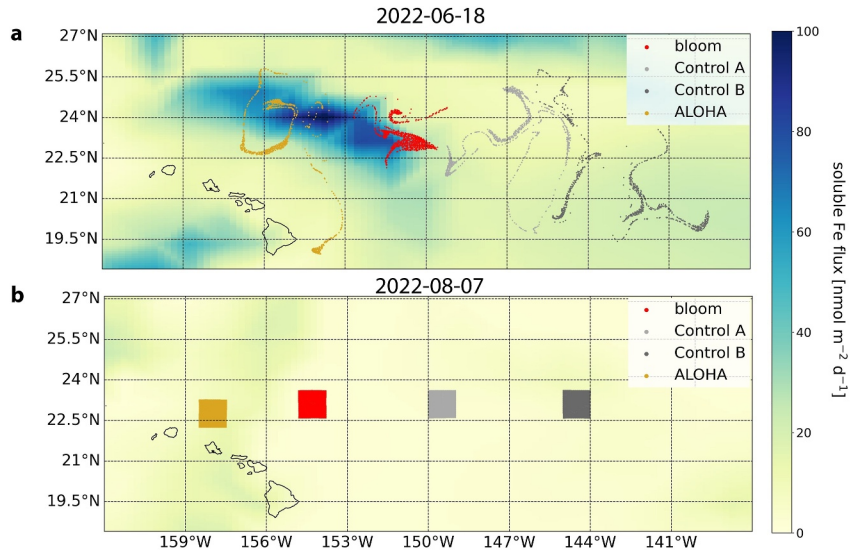

Figure 3. Map view of daily modeled aerosol soluble Fe deposition rates from the Mechanism of Intermediate complexity for Modeling Iron (MIMI) model with the locations of the 900 parcels from each back trajectory group for a day during the pulse of particularly high soluble Fe deposition approximately 4 weeks before the initiation of the bloom (a), and a day during the height of the 2022 bloom on which back trajectory groups were initialized (b).

et al. (2019). MIMI estimates Fe emissions and their atmospheric processing from mineral dust, anthropogenic activity, and biomass burning. The model includes parametrizations for Fe aerosol dissolution via acidic interstitial reactions and in-cloud processing with oxalate. The model is constrained based on Fe solubility observations from different leaching media in aerosols (Bergas-Masso et al., 2025). Meteorology was nudged to Modern-Era Retrospective analysis for Research and Applications (MERRA2). Daily wet and dry deposition fluxes to the surface ocean were obtained at the model resolution of 1.25° × 0.9° (longitude by latitude), and initially reported on kg m^{-2} s^{-1} and then converted to nmol m^{-2} d^{-1} to determine daily deposition rates.

In all simulations, desert dust was represented using the Dust Entrainment and Deposition module (Zender et al., 2003) with several key updates. These include incorporation of dust mineral composition (Scanza et al., 2015), brittle fragmentation theory for mineral size distributions (Kok, 2011; Scanza et al., 2015), a physically based parameterization for vertical dust flux (Kok et al., 2014), and the influence of particle asphericity on dust mass extinction efficiency (Kok et al., 2017). The global annual mean dust aerosol optical depth was adjusted to 0.03, consistent with observational constraints (Ridley et al., 2016). Fire emissions follow the Quick Fire Emissions Data Set (QFED) (Darmenov & Silva, 2015). For CESM, these emissions are calculated as a product of the QFED CO_2 emission fields and relevant aerosol or gas emission ratio for the Fire INventory from NCAR (FINN) inventory (Wiedinmyer et al., 2011). The MIMI model was driven by the anthropogenic emissions data set described by Rathod et al. (2020), which was updated by Hamilton et al. (2020) to incorporate a transient trend based on anthropogenic black carbon emissions. This results in anthropogenic soluble Fe deposition fluxes in August on parity with mineral dust in the North Pacific by 2015 (Hamilton et al., 2020).

We used MIMI to assess whether enhanced Fe deposition may have contributed to the seeding of the 2022 bloom in the study region. The model provides high-resolution daily estimates of both soluble and total Fe deposition, enabling quantification of the short-term response to primary productivity from a region that is thought to be sensitive to intermittent inputs of aerosols over the summer. The daily locations of each parcel in the back trajectory simulations were matched with the nearest soluble Fe deposition rate at that specific time to create the history of soluble Fe deposition of surface waters that were transported to the bloom or control locations on 7 August 2022 (Python code available at https://github.com/philkongo/chl_mimi_backtraj_match, accessed 22 July 2022). For the four zones within the study area, 900 simulated water parcel back-trajectories were generated to determine the Lagrangian history of soluble Fe deposition of parcels that ended up at the four zones in our study area (Figure 3). The parcels within each zone were evenly spread within a 1° by 1° box. The locations of each parcel were updated daily for 75 days dating back to 24 May 2022, and daily soluble Fe deposition fluxes were

compiled for each parcel by pairing the daily location of each water parcel to the corresponding chlorophyll *a* concentration data. The daily soluble Fe deposition flux time series was then calculated for each zone by determining the average soluble Fe deposition rates of the 900 parcels for each day. The matching algorithm was compiled using a high-performance computing system provided by The Center of Advanced Research Computing (CARC) at USC.

Weekly estimates of soluble Fe deposition from the entire study area were also conducted to a broader spatio-temporal analysis, where back trajectory analyses of 1,800 parcels were evenly distributed within 20°N to 30°N, 160°W to 140°W. Soluble Fe deposition was matched to the daily locations of each of the parcels in the back trajectory analysis for 75 days. Maps of weekly cumulative soluble Fe deposition along water parcel back trajectories were then created to determine the cumulative deposition of soluble Fe on water parcels within the entire region on 7 August 2022.

2.5. Satellite Chlorophyll Observations

Chlorophyll *a* concentrations from the study area (20°–30°N, 140°–164°W) were evaluated using Copernicus Globcolour Level 4 data from June 2003 to August 2022 (CMEMS, 2025). The level 4 data is spatially interpolated daily to obtain gap free measurements of chlorophyll *a* at a 4-km resolution. Concentrations of chlorophyll *a* from satellite observations were matched with locations from each back trajectory simulation. In the same way that average soluble Fe deposition was determined along back trajectories initiated within the four zones of interest (Section 2.4), we evaluated the Lagrangian histories of chlorophyll *a* by matching the interpolated satellite chlorophyll *a* measurements to the locations of the back trajectory model for each zone. The daily locations of 900 parcels from the back trajectory analysis from each zone were matched with the nearest available chlorophyll *a* concentrations over a 75-day period.

3. Results

3.1. Fe, Al Concentrations, and Fe Stable Isotopes in the 2022 Bloom

3.1.1. Dissolved and Suspended Particulate Fe Concentrations and Isotopes

The dFe concentration profile within the 2022 bloom was similar to previous observations of dFe in the NPSG with the exception of elevated concentrations within the bloom core located between 0 and 80 m below the surface (Figure 4a, Foreman et al., 2025). Within the 2022 bloom, dFe concentrations were 0.50 and 0.75 nM at 15 and 75 m, respectively, significantly higher than the mean summer dFe concentration (0.33 nM) within the same depth range at Station ALOHA (Bates & Hawco, 2025; Boyle et al., 2005; Brown et al., 2005; Bruland et al., 1994; Bundy et al., 2018; Fitzsimmons et al., 2015; Hawco et al., 2021, 2022). The dFe concentration at 75 m is the third highest surface value reported during the summer months near Station ALOHA; the highest value of 0.874 nmol/kg was reported in August 2013 (Fitzsimmons et al., 2015). Typically, dFe concentrations at the surface are expected to be low during the summer months when aerosol Fe inputs are at their lowest (Hamilton et al., 2020), but episodic dust deposition at Station ALOHA has been shown to increase surface dFe concentrations (Fitzsimmons et al., 2015). Below the surface, dFe was depleted to its minimum concentrations of 0.14–0.24 nM in the water column between 100 and 150 m (Figure 4a). The depth of the dFe local minimum is consistent with previously reported observations at Station ALOHA that is typically coincident with the deep chlorophyll maximum (DCM); the dFe concentration at this minimum in the 2022 bloom was approximately 2 times higher than average dFe concentrations reported at Station ALOHA (Fitzsimmons et al., 2015; Hawco et al., 2022). Within the 2022 bloom, excess biomass at the bloom core shaded solar light penetration within the bloom and the chlorophyll *a* maximum shoaled up to ∼50 m while the dFe minimum remained near 100 m (Foreman et al., 2025).

Suspended pFe concentrations within the bloom core ranged from 0.16 to 0.21 nM, similar to previously reported suspended pFe concentrations at Station ALOHA (Figure 4b; Boyle et al., 2005; Hawco et al., 2022; Lam et al., 2024; Bates et al., 2025). The highest reported surface suspended pFe concentration at Station ALOHA was 0.26 nM at 25 m collected in June 2019 (Hawco et al., 2022). Below the bloom core, suspended pFe concentrations within the 2022 bloom gradually increased to reach a maximum at 200 m to 0.49 nM, and decreased to 0.12 nM at 500 m (Figure 4b). The suspended pFe profile from the 2022 bloom follows a similar trend observed at

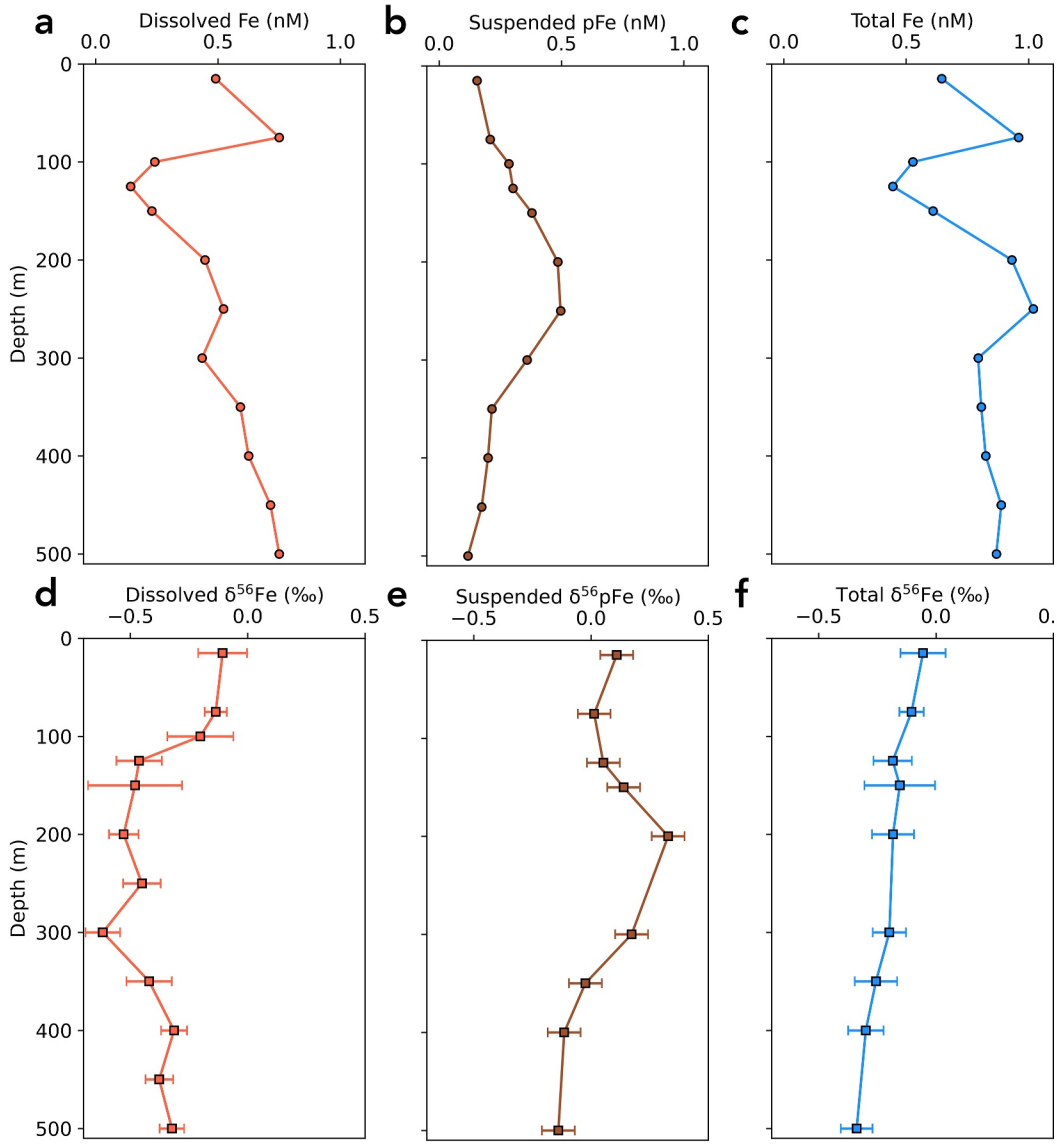

Figure 4. Profiles of dissolved Fe (a) suspended particulate Fe (pFe; b), total Fe concentrations (c), and their respective stable isotope profiles (d–f) within the 2022 bloom.

Station ALOHA in October 2018, where the upper mesopelagic maxima of 0.20 nM was located at 146 m (Lam et al., 2024).

The isotopic signature of Fe in the dissolved phase and suspended particulate phase in the surface waters of the 2022 bloom span a tight range from −0.2‰ to 0.2‰, which coincides with the Fe isotopic composition of dust from the atmosphere (Figures 3b, 3d, and 5b; Fitzsimmons & Conway, 2022). Dissolved Fe concentrations reach a minimum below the bloom core at 100 m and dissolved δ^{56}Fe reach a minimum at mid-depths (100–300 m, Figures 4a and 4d). Lighter δ^{56}Fe signatures were observed below the surface at Station ALOHA in the GP15 cruise, where the δ^{56}Fe ratio ranged between −0.02‰ and −0.54‰ from 130 to 450 m (Conway et al., 2022). Where the δ^{56}Fe signatures for dFe were light, δ^{56}pFe had contrasting heavier signatures (Figures 4d and 4e).

The total Fe concentration (dissolved + particulate) signature strongly reflects the dissolved signature, as the dissolved phase constitutes most of the measured total Fe signature in the 2022 bloom (Figures 4a–4c). With the exception of the dissolved minima between 100 and 150 m (Figure 4a), the total Fe profile has a uniform concentration of ∼0.75 nM in the observed water column (Figure 4c). Similarly, the combined contrasting patterns in

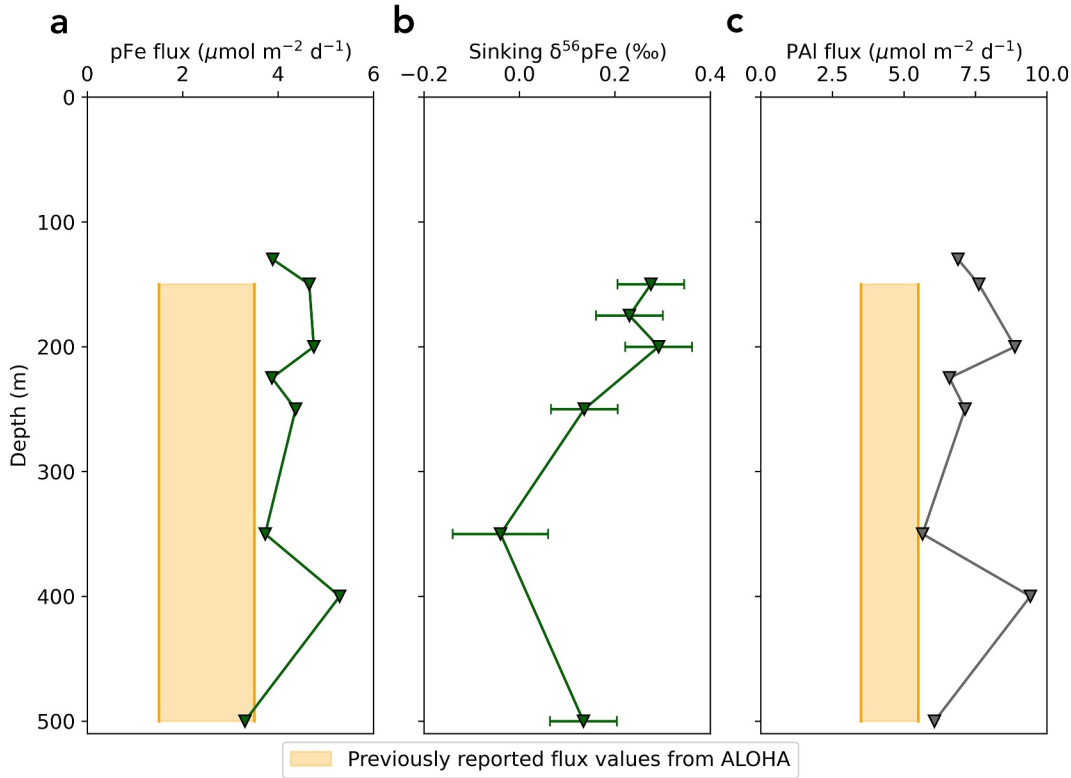

Figure 5. Sediment trap flux of sinking particulate Fe (a), the isotopic composition Fe in sinking particles (b), and fluxes of sinking particulate Al (c) within the June 2022 bloom. The yellow bar represents the range of previously reported elemental flux values at Station ALOHA, from Lamborg et al. (2008), Hawco et al. (2022).

the dissolved and particulate phases (Figures 4d and 4e) result in a total δ^{56}Fe signature that is invariant with depths between 0 and 200 m (Figure 4f). Below 200 m, we observed a subsurface excursion to lighter total δ^{56}Fe values that coincides with light δ^{56}Fe of dFe and pFe (Figures 4d, 4e, and 4f).

3.1.2. Suspended Particulate Aluminum Concentrations

Suspended particulate aluminum (pAl) concentrations ranged from 0.26 nM at the surface to 0.96 nM at 500 m, which are similar to observations previously reported in the NPSG that range from 0.1 to 1.5 nM (Figure S2 in Supporting Information S1; Lam et al., 2024; Orians & Bruland, 1986) The elemental ratio of suspended pFe to suspended pAl (Fe:Al) at the surface is 0.59, comparable to the Fe:Al ratio of aerosols (0.47) collected at Hawai'I Volcanoes National Park in July 2022 (Figure S2 in Supporting Information S1; Malm et al., 1994).

3.1.3. Sinking Particulate Metal Fluxes

Sinking pFe fluxes within the 2022 bloom remain relatively constant below 100 m (Figure 5a). Sinking Fe fluxes averaged 4.07 ± 0.86 mmol m^{-2} d^{-1}, and were greater than median fluxes previously reported at Station ALOHA by 35% (Hawco et al., 2022; Lamborg et al., 2008). Sinking fluxes of pAl were also relatively constant with depth, with an average of 7.04 ± 1.79 mmol m^{-2} d^{-1}, which was 41% higher compared to median fluxes observed at Station ALOHA (Figure 5c). Elevated fluxes of Fe and Al below the 2022 bloom could be due to elevated input of aerosol particles to the waters where the bloom formed. For all depths within the bloom, the average Fe:Al was 0.58 ± 0.05 mol mol^{-1}, which was slightly enriched in Fe compared to values previously reported at Station ALOHA (Hawco et al., 2022; Lamborg et al., 2008). We can estimate the rate of lithogenic aerosol deposition to the 2022 bloom location to be 2.09 ± 0.32 mg m^{-2} d^{-1} with the assumption that Al makes up 8% of the upper continental crust. Such lithogenic aerosol deposition rates are higher than those calculated for June 2019 by ∼60%, further supporting an increased supply of aerosols delivered to the 2022 bloom (Hawco et al., 2022; McLennan, 2001). The isotopic composition of sinking particles between 150 and 500 m ranged between

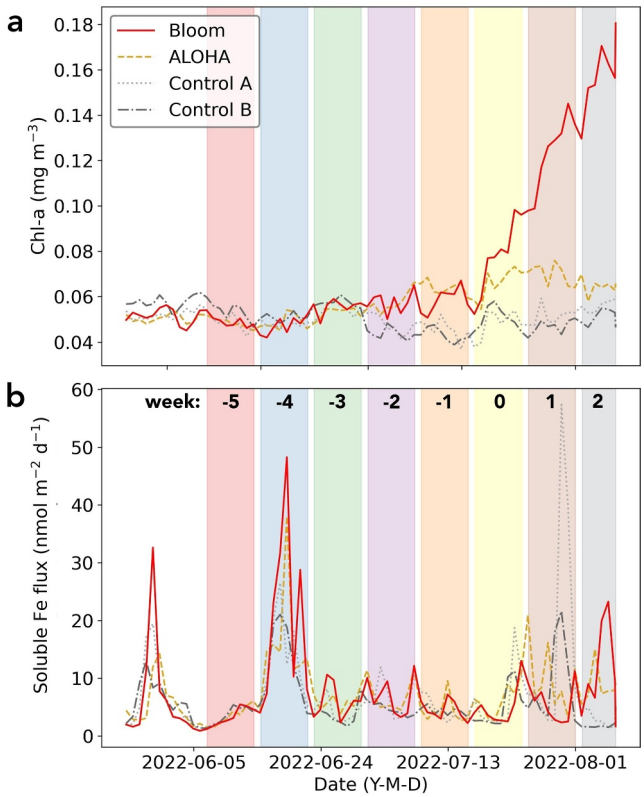

Figure 6. Mean surface chlorophyll *a* concentration of the daily locations of 900 parcels initialized from the bloom site and three control sites (a). Mean surface deposition flux of soluble aerosol soluble Fe on the daily locations of 900 parcels within each back trajectory group (b). Shaded regions in the two panels correspond to the week from the time the 2022 bloom formed.

−0.03‰ and 0.29‰ (Figure 5b), and its pattern strongly resembled that of the suspended pFe, which ranged from 0.13‰ to 0.32‰ between 150 and 500 m (Figure 4e).

3.2. Satellite Chlorophyll *a*

Following the redefined parameters for blooms in the central NPSG (where blooms in the NPSG are defined as having chlorophyll *a* concentrations exceeding 0.09 mg m^{-3} and remaining contained within the same geographic vicinity), the 2022 bloom started on 13 July near 22°N, 155°W and remained active until 6 October (Foreman et al., 2025). At its peak, the bloom reached an aerial extent greater than 220,000 km^2, and the highest observed satellite chlorophyll *a* concentration measurement during its peak was 0.25 mg m^{-3} (Foreman et al., 2025).

Satellite chlorophyll *a* observations of surface waters along the parcel back trajectory simulations also show a dramatic increase around 13 July. The average chlorophyll *a* concentration of the parcels that ended up in the 2022 bloom zone rapidly increased starting 13 July and exceeded 0.09 mg m^{-3} in mid-July. Within the bloom, chlorophyll *a* concentrations gradually increased to 0.18 mg m^{-3} on 7 August (Figure 6a). Conversely, chlorophyll *a* concentrations of back trajectory parcels that originated from other zones in this study, including Station ALOHA (22.5°N, 158.0°W), Control A (23.3°N, 149.6°W), and Control B (23.3°N, 144.6°W), had surface chlorophyll *a* concentrations between 0.04 and 0.06 mg m^{-3}, values consistent with the typical chlorophyll *a* concentrations during the summertime at Station ALOHA.

Chlorophyll *a* patterns were also assessed over interannual timescales by determining the chlorophyll *a* concentrations along back trajectories that were initialized from the 2022 bloom location over 20 summers starting in 2003. While there were both daily and interannual variability for every year, the highest chlorophyll *a* concentrations measured were in back trajectory parcels that originated from the location of the 2022 bloom (Figure 7a).

3.3. Fe Deposition Fluxes During the Summer of 2022

3.3.1. General Patterns in Fe Deposition Flux Within the Study Area

Deposition fluxes of soluble Fe within our study area (20°–30°N, 140°–164°W) were quite dynamic with high daily variability, as Fe deposition fluxes are impacted by dust mineralogy, atmospheric processing, and the climactic conditions at the specific location. Within the study area, the mean daily total Fe deposition flux from the MIMI model for the early summer months (June and July) in 2022 was 209.47 ± 38.18 nmol m^{-2} d^{-1} (Figure 8). The soluble Fe deposition flux was much less than the total, with a mean value of 8.12 ± 1.23 nmol m^{-2} d^{-1} for the same period. This represents a 3.9% solubility of Fe deposited in our study area, similar to observations of Fe solubility from previous studies conducted in the study area (Buck et al., 2006, 2013; Measures et al., 2010).

Though localized daily deposition rates vary over orders of magnitude (Hamilton et al., 2019), the seasonality of total dust deposition at the regional scale is generally similar year-to-year (Hamilton et al., 2020). For each of the early summer months between 2019 and 2022, the daily average total and soluble Fe deposition rates from the MIMI were 250.08 ± 35.51 and 7.92 ± 0.67 nmol m^{-2} d^{-1} respectively (Figure 8). Much of the deposition occurring in the study region is driven by events that deposit large amounts of total and soluble Fe on small timescales; for example, the 2022 bloom pulse event deposited 6.3 times more soluble Fe than the average deposition rates during our study period (Figure 6b). Over each of the early summer months from 2019 to 2022, approximately 10% of the days had Fe deposition rates greater than 1 standard deviation above the mean each year; yet these days accounted for 38%–48% of the sum total of soluble Fe deposition (Figure 8).

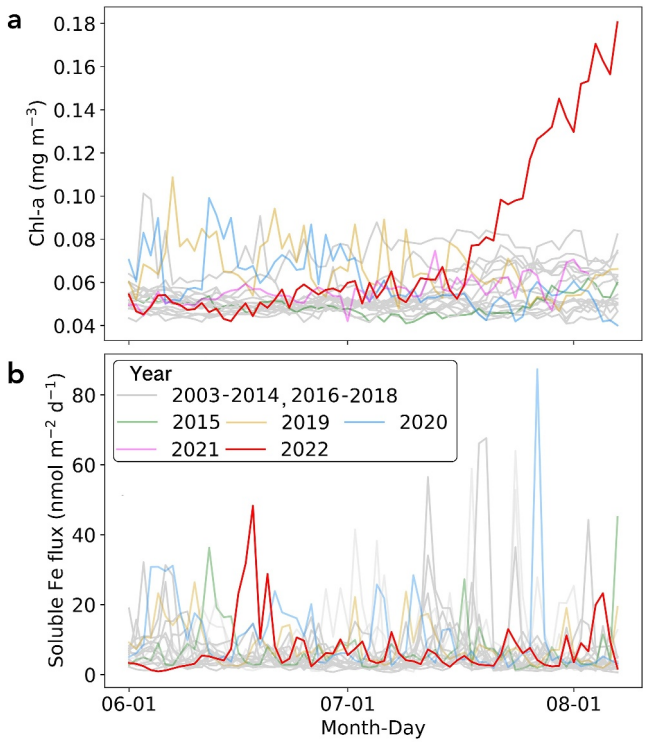

Figure 7. Mean surface chlorophyll *a* concentration of the daily locations of 900 water parcels initialized from the 2022 bloom site between 2003 and 2022 (a). Specific years where high levels of deposition were observed have been highlighted with colored lines. Mean surface deposition flux of total aerosol soluble Fe on the daily locations of 900 parcels initialized each year from the bloom site between 2003 and 2022 (b).

3.3.2. Fe Deposition Along Back-Trajectories

We evaluated soluble Fe deposition along advected back trajectories of water parcels to determine the history of Fe deposition along surfaces that passed through the bloom's location and three other zones where the bloom did not form. The typical background deposition flux values of back trajectories for all zones ranged between 5 and 10 nmol m^{-2} day^{-1} and reflect the typical dry deposition fluxes in this study area (Figure 6b). In addition to days of lower deposition fluxes, back trajectory histories of soluble Fe deposition along the four back trajectory groups show irregular patterns of elevated fluxes typically lasting several days (Figure 6b).

These events of higher deposition, henceforth referred to as deposition pulses, contributed a significant portion of soluble Fe deposition along the back trajectories of the 75-day period. The largest deposition pulse occurred 4 weeks ($t_{-4\ \mathrm{weeks}}$) prior to the formation of the bloom from 17 June 2022 to 23 June 2022 (Figure 6b). Soluble Fe deposition fluxes along the bloom back trajectory reached up to 50 nmol m^{-2} d^{-1}, almost one order of magnitude higher than the background levels for water parcels that ended up at the bloom. During this event, soluble Fe fluxes spiked over a 5-day pulse, delivering a total of 158 nmol m^{-2} of soluble Fe on waters that were transported to the bloom's site after $t_{-4\ \mathrm{weeks}}$. While this pulse deposited higher levels of soluble Fe on water parcels that did not end up at the bloom's site, the bloom back trajectory parcels received the most soluble Fe among the back trajectory groups evaluated in this study. The pulse event deposited 1.3 to 1.7 times more soluble Fe on bloom water than they did to the water parcels where the bloom did not form (Table S5 in Supporting Information S1).

The high fluxes of Fe deposition $t_{-4\ \mathrm{weeks}}$ prior to the formation of the bloom are attributable to wet deposition. In that week, wet deposition accounted for 78% of soluble Fe deposition along the bloom back trajectory, compared to the average wet deposition contribution of 45% in the early summer months between 2019 and 2022 (Figure S4 in Supporting Information S1). A map of precipitation rates from the NASA's Integrated Multi-satellitE Retrievals for GPM (IMERG) product (Huffman et al., 2019) were compared with the map of soluble Fe deposition of the study area on the same day. Precipitation events coincide well with the locations of elevated high soluble Fe deposition (Figure S3 in Supporting Information S1). Given that wet deposition made up much of the soluble Fe deposition in our analysis, we conclude that precipitation events control large pulses of Fe deposition in our study area.

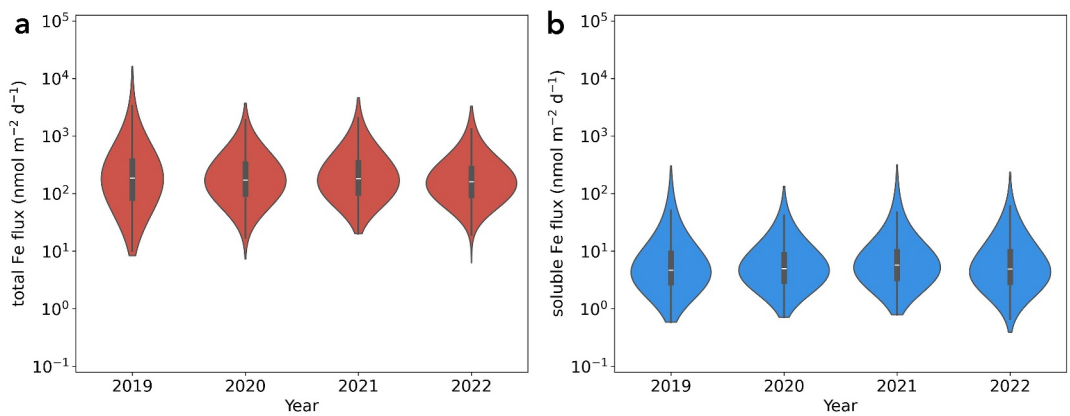

Figure 8. Modeled daily total Fe deposition fluxes (a) and daily soluble Fe deposition fluxes (b) within the study region (20°–30°N 140°–164°W) between June and July of each year. The width of each band reflects the frequency of days with Fe deposition of that magnitude.

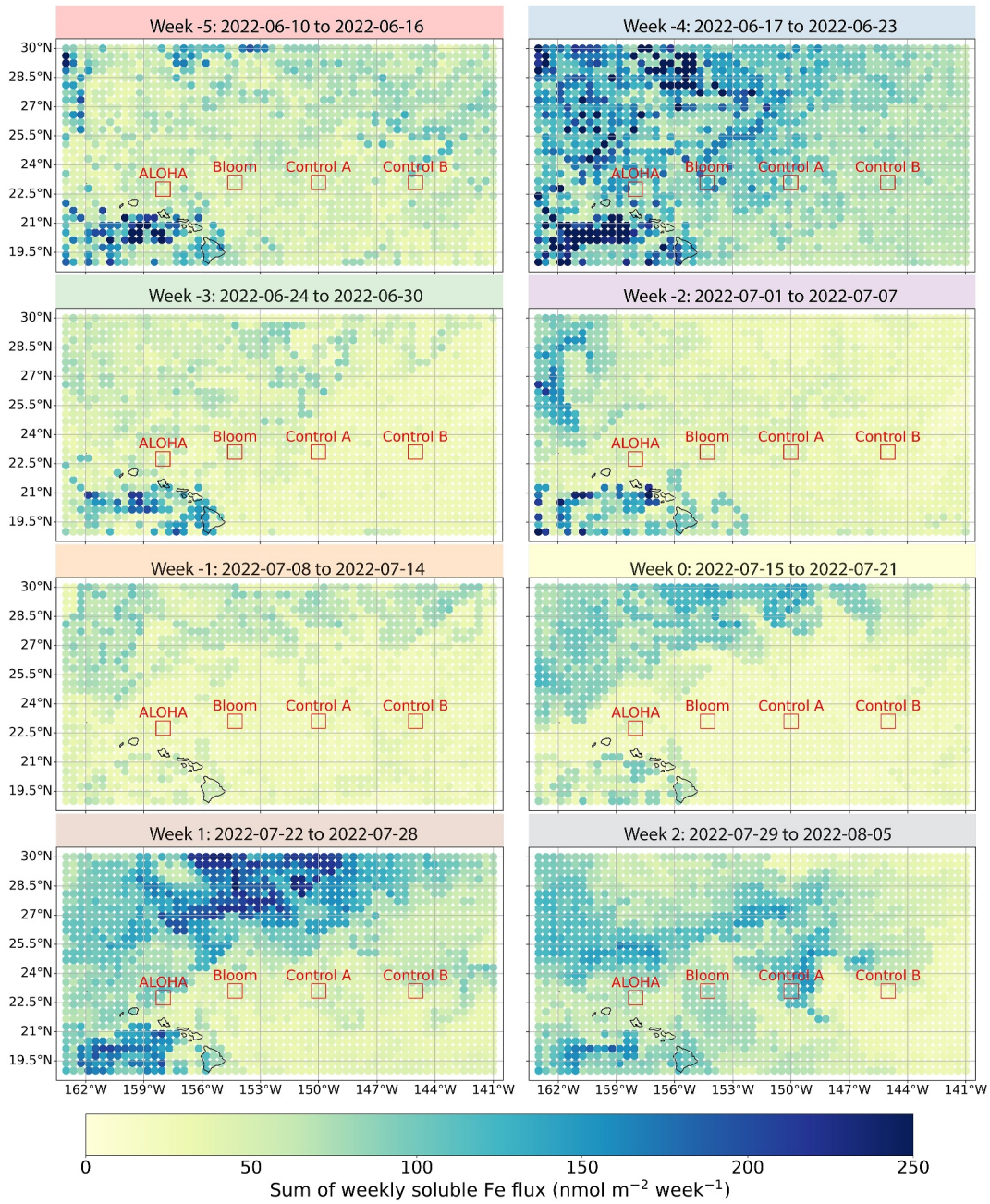

Figure 9. Weekly soluble Fe deposition from aerosols on the surface ocean during the 2022 bloom's onset and growth. The position of each circle represents the location of a water parcel on 7 August 2022, while the color of these circles reflects the weekly sum of Fe deposition which occurred along the back-trajectory of that parcel before it reached this location. Red squares show the locations of the bloom and three control back trajectory zones outlined in Figure 1.

3.3.3. Spatiotemporal Analyses of Soluble Fe Deposition

We can consider the historical patterns in soluble Fe deposition from a broader spatiotemporal perspective by looking at the weekly patterns in soluble Fe deposition across the region. This exercise of comparing cumulative weekly deposition rates instead of daily rates in our study area reduces uncertainties in the MIMI model's deposition flux estimates. Plots of weekly cumulative distributions of soluble Fe deposition confirm that very little soluble Fe is delivered to the surface ocean in this region outside of specific periods where episodes of wet deposition occur (Figure 9). In the fourth week prior to the formation of the 2022 bloom, higher levels of soluble

Fe were deposited throughout the entire study area, not just on the surface waters that ended up at the bloom. It is evident that the storm event did not only deposit soluble Fe on the ocean surface that ended up at the 2022 bloom's location; rather, the rainfall event deposited and dispersed high levels of Fe around a large region of the study area (Figure 9).

3.4. Relationship Between Fe Deposition and Chlorophyll From 2003 Through 2022

We also assessed the interannual variability in soluble Fe deposition fluxes at the bloom's location. Soluble Fe deposition fluxes along back trajectory analyses were determined from the location of the 2022 bloom, starting each year on 7 August from 2003 to 2022. Unlike the chlorophyll *a* history of the bloom location between 2003 and 2022, soluble Fe deposition fluxes along the back trajectory parcels from 2003 to 2022 were variable year to year (Figure 7b). There were deposition fluxes in some years higher than those in 2022 that were driven by wet deposition events. However, no other high deposition event led to the production of phytoplankton that was observable by satellite. As evidenced by the spatiotemporal analyses conducted for the 2022 bloom, the growth of diazotrophs may require more than just soluble Fe deposition on the water parcels; other factors such as phosphorus availability, climatological conditions, sea level pressure, and biological transport of nutrients likely play a role in the growth of nitrogen fixing microbes (Letelier et al., 2019).

4. Discussion

4.1. The 2022 Bloom Was Enriched in Fe From Aerosols

Late summer blooms near Station ALOHA occur during periods when N_2 fixation rates contribute to a significant portion of surface-ocean nitrogen, linking Fe to the formation of blooms in the NPSG (Böttjer et al., 2017; Grabowski et al., 2008; Mills et al., 2004; Vitousek & Howarth, 1991). The 2022 bloom was enriched in cell counts of the diatom *Hemiaulus* and its diazotrophic symbiont *Richelia* (Foreman et al., 2025); both taxa are prone to Fe stress under typical NPSG conditions, each due to distinct physiological demands (Bundy et al., 2018). *Hemiaulus's* relatively large cell size elevates its overall Fe requirement for growth and photosynthesis (Bundy et al., 2018; Harke et al., 2019; Twining & Baines, 2013), whereas *Richelia's* reliance on its Fe rich nitrogenase system drives its high Fe demand for N_2 fixation (Harke et al., 2019). The total concentrations of Fe, defined here as the sum of dissolved and particulate Fe, measured in the 2022 bloom core (0–80 m) had the highest value reported near Station ALOHA in the summer months (Figure 3, Table S4 in Supporting Information S1). The relative surplus of Fe compared to other years may have provided the requisite Fe to facilitate the high levels of N_2 fixation observed in the 2022 bloom (Karl, 2002; Letelier et al., 2019). Decades of research has established that aerosol Fe can help stimulate the formation of late summertime phytoplankton blooms in the NPSG (Dore et al., 2008; Duce & Tindale, 1991; Martin & Fitzwater, 1988). The same may be true for the 2022 bloom, as evidence presented here suggests that aerosol deposition was the dominant source of Fe.

Sinking fluxes and elemental ratio particles suggest that the elevated concentrations of Fe delivered to the 2022 bloom core originated from atmospheric input. Fluxes of Fe and Al from particles collected on sediment traps were significantly elevated than those under non-bloom conditions at Station ALOHA (Figures 5a and 5c). Sinking fluxes of Fe and Al also exhibited a strong vertical correlation (Pearson's $r = 0.93$, $p < 0.001$), implying that the sinking particle composition remained constant with depth. The Fe:Al ratio of suspended particles and sinking particles collected on August 2022 in the bloom core were 0.59 and 0.56 mol:mol, respectively, virtually identical to the average Fe:Al ratio of 0.54 from aerosol particles collected at the Hawaii Volcanoes National Park (19.431°N, −155.258°W) from June to August 2022 (Malm et al., 1994). These ratios are consistent with Fe:Al measurements of sinking particles from Station ALOHA during the summer despite using a different solution to digest particles in this study (Hawco et al., 2022; Lamborg et al., 2008). Reported Fe:Al ratios of seawater particles near the Hawaiian Islands are significantly enriched in Fe compared to the bulk upper continental crust Fe:Al (Rudnick & Gao, 2014) and aerosols collected in October 2018 near Station ALOHA (Marsay et al., 2022). We employed a particle digestion method that does not dissolve all recalcitrant lithogenic elements such as Al and Ti; therefore, we cannot be certain that total particulate metals from within the 2022 bloom have the same signature as those from Hawaii Volcanoes National Park (Table S2 in Supporting Information S1, Planquette & Sherrell, 2012). However, the similarity of our Fe:Al ratios to those of analogous particles subjected to total digestion suggests that our samples are relatively depleted in refractory Al and Ti compared with particles collected closer to their source regions (Lam et al., 2018; Marsay et al., 2022). It is plausible that the similarities

observed in the Fe:Al ratios of seawater and aerosol particles are not merely coincidental, and the composition of seawater in the 2022 bloom closely resembles that of aerosols collected in nearby regions.

The isotopic composition of Fe measured in the 2022 bloom provides further evidence for an aerosol source of Fe. The δ^{56}Fe compositions of total Fe in the bloom core range from −0.1‰ to −0.05‰ (Figure 4f). The typical range of δ^{56}Fe for aerosols ranges between −2.2‰ and 0.5‰ (Fitzsimmons & Conway, 2022), with contributions from a mixture of lithogenic (δ^{56}Fe ≈ +0.1‰), pyrogenic (δ^{56}Fe ≈ −1.6‰ to +0.8‰), and anthropogenic (δ^{56}Fe ≈ −4.3‰ to −1.6‰) sources (Bunnell et al., 2025; Conway et al., 2019; Kurisu et al., 2019). Considering wind patterns in the North Pacific, aerosols delivered to the 2022 bloom likely contained Fe that originated from both Asia and North America (Kok et al., 2021; Marsay et al., 2022). In the 10 weeks leading up to the bloom, over 50% of the soluble Fe deposited on surface waters that ended up at the 2022 bloom originated from pyrogenic and anthropogenic sources (Figure S4 and Table S5 in Supporting Information S1). Using estimated contributions from MIMI for each Fe source and constrained δ^{56}Fe end-member values for soluble and total Fe in aerosols from the NPSG (Bunnell et al., 2025), we calculated an expected δ^{56}Fe composition of −0.12‰ for the soluble fraction and 0.06‰ for the total fraction within the 2022 bloom. The expected values lie within the average measured total δ^{56}Fe value of −0.08‰ in the bloom core (Figure 4f). Assuming a linear mixing relationship between the soluble and total phases of Fe, we estimate that the dissolved and suspended Fe in the surface of the bloom comprised of 79% soluble Fe and 21% recalcitrant Fe. The majority of the recalcitrant aerosol Fe likely sank out of the water column or were advected out of this region upon entering the water column. This is corroborated by a heavier Fe isotope composition of sinking particles captured on sediment traps, where the δ^{56}Fe ranged between −0.03 and 0.29‰ (Figure 5b). The δ^{56}Fe values of surface dissolved and particulate Fe within the 2022 bloom were lighter than those from comparable aerosol samples collected in summer 2013 near the Hawaiian Islands, which were interpreted to be predominantly lithogenic Fe (Kurisu et al., 2021). Independent models also confirm that the composition of aerosols near the Hawaiian Islands is typically expected to have a lithogenic source with less than 20% contribution from pyrogenic/anthropogenic aerosols (Hamilton et al., 2019). In contrast, the lighter Fe isotopic signature detected in the 2022 bloom is consistent with pulses of substantially enhanced input from pyrogenic and anthropogenic aerosols, known to supply more bioavailable forms of Fe (Mead et al., 2013; Schroth et al., 2009; Sholkovitz et al., 2009; Trapp et al., 2010). This augmented supply of bioavailable Fe likely supported diazotroph and phytoplankton productivity, ultimately triggering the 2022 bloom.

The highly stratified summer conditions in the NPSG and direction of surface water advection indicate that diapycnal mixing and lateral fluxes did not play an important role in supplying Fe to the surface ocean, further suggesting that aerosol input was the primary source of Fe in this study area. The potential density measurements of the 2022 bloom reported by Foreman et al. (2025) indicate marked stratification in the upper water column, which implies limited vertical supply of Fe through mixing of surface water with deeper, Fe-rich waters. Furthermore, surface waters within the 2022 bloom were advected from the east, where no known Fe sources such as land masses, continental shelves, or hydrothermal plumes exist (Figure S1 in Supporting Information S1).

It has been established for many decades that dust fluxes in the NPSG are highest during the spring months (March to May), when approximately 78% of annual dust is delivered to surface waters (Ohnemus et al., 2025). Dust storm events during the spring have led to discernible increases in primary productivity (DiTullio & Laws, 1991). While the highest spring aerosol deposition fluxes in two decades occurred in 2022, this dust event did not result in an immediate increase in primary production in nearby surface waters (Ohnemus et al., 2025). Although Fe in the upper euphotic zone has a residence time of approximately six months (Hawco et al., 2022), it is unclear if the 2022 spring dust pulse contributed requisite nutrients to the 2022 bloom since surface water transport is dynamic in this region. Studies of previous blooms in the NPSG have not been able to identify a clear correlation between springtime dust and summertime blooms near Station ALOHA (Calil et al., 2011; C. Wilson, 2003, 2021). Furthermore, given the significant time gap between the episodic springtime dust deposition events that annually peak in the third week of April (Ohnemus et al., 2025) and the likelihood that sinking lithogenic pFe and ballasted particles were exported rapidly in dust-rich seasons, more recent deposition of Fe that had not already been exported out likely contributed to the elevated Fe signature in the 2022 bloom core. Despite similar summertime aerosol Fe deposition fluxes from 2019 to 2022 in our study area (Figure 8), a large bloom only occurred in 2022, suggesting that drivers of Fe solubility—namely aerosol composition, transport pathway, and deposition timing—control the formation of summertime DDA blooms in the NPSG. These factors are modulated by regional climatology and must be strongly considered to better understand the inception of blooms in the NPSG (Letelier et al., 2019).

4.2. Pulses of Aerosol Fe Deposition Contribute to a High Summer 2022 Fe Inventory

Our Lagrangian analysis reveals that short but intense pulses of wet deposition were the primary mechanism for the delivery of aerosol Fe to the surface waters of the 2022 bloom. Soluble Fe flux estimates from the MIMI model show that wet deposition delivered 59% of soluble Fe to the water parcels that seeded the 2022 bloom during the month preceding its onset (Figure S4 and Table S6 in Supporting Information S1). Relative to dry deposition, rain events supply larger amounts of soluble Fe over shorter timescales (Chow et al., 2025; Karl et al., 2021; Ohnemus et al., 2025). The deposited soluble Fe, which is present as both dissolved and particulate Fe, is readily accessible to diazotrophs (Zehr & Capone, 2020). While dFe is more bioavailable than pFe, some diazotrophs such as *Trichodesmium* can directly utilize pFe to sustain growth (Achilles et al., 2003; Rubin et al., 2011). Consequently, episodic wet deposition pulses provide a mechanistic link between atmospheric Fe supply, enhanced N_2 fixation, and the subsequent increase in primary productivity in the NPSG.

Moreover, the timing and location of wet deposition pulses were critical in initiating the 2022 bloom. A pair of substantial rain events that occurred $t_{\text{-4 weeks}}$ prior to the bloom's onset delivered 49% of the total soluble Fe deposited in the 30 days preceding the bloom (Figure 6b, Figure S3 in Supporting Information S1). Notably, this 5-day pulse alone contributed 28% of the total soluble Fe deposition over the entire 10-week study period (22 May 2022 to 7 August 2022; Figure 6b). Such concentrated inputs of soluble Fe may help overcome the typically limiting conditions of low nutrient availability and sparse biomass, thereby promoting nitrogen fixation and primary production in surface waters of the NPSG (Dore et al., 2008; Karl, 2002).

Emerging evidence indicates a temporal lag of several weeks between nutrient input and the resulting increase in biomass in the NPSG. Incubation studies demonstrate that nitrogen fixation activity can remain slow for 3–4 weeks before accelerating after nutrient input (Chow et al., 2025; Seelen et al., 2025). Consistent with lab incubations, both satellite observations and in situ measurements reveal a similar temporal offset between atmospheric deposition of variable aerosol material, biological assimilation, and the subsequent export of newly fixed N by diazotrophs (Chow et al., 2025; Church et al., 2009). The 2022 bloom also exemplifies this pattern: a major wet deposition event pulse of soluble Fe was followed by a sharp increase in primary productivity several weeks later, suggesting that the timing of nutrient delivery may be a key factor in influencing the formation of summer blooms in the NPSG (Figures 6a and 6b).

Several factors could account for the month-long lag between the deposition of soluble Fe and the corresponding biological response from diazotrophs. Key diazotrophic controls such as P availability (Karl, 2002; Letelier et al., 2019; Sohm, Subramaniam, et al., 2011), surface hydrographic conditions (Böttjer et al., 2017; Church et al., 2009; Fong et al., 2008), and sea surface temperature (Figure S5 in Supporting Information S1; Jiang et al., 2018; Yang et al., 2021) may have aligned with the wet deposition event to stimulate nitrogen fixation activity. Particulate Fe can dissolve gradually through photoreduction of Fe minerals or be assimilated steadily by microorganisms, leading to progressive increases in biomass over time (Basu et al., 2019; Kranzler et al., 2016; Rubin et al., 2011; Waite & Morel, 1984). Given Fe surface residence times of approximately 6 months in the upper euphotic zone (Hawco et al., 2022), extensive recycling of Fe observed in the surface waters of the NPSG may give rise to forms of Fe which are more bioavailable to diazotrophs, for example, through the production of siderophores or other biological ligands (Amin et al., 2009; Boyd et al., 2010). Finally, even if the delivery of Fe led immediately to conditions favorable for diazotroph growth, it may have taken time for their abundance to increase from a small initial seed population.

The $t_{\text{-4 weeks}}$ pulse added a significant amount of soluble Fe to the surface of the 2022 bloom, depositing at least 28% more soluble Fe on the bloom back trajectory parcels than the storm did on other control zones in our study (Table S3 in Supporting Information S1). While the bloom zone did receive more soluble Fe deposition than the other discrete zones tested (ALOHA, Control A, and Control B), surface waters that received significant amounts of soluble Fe also dispersed to other regions of the study area where large blooms did not occur (Figure 9). Consequently, pulses of soluble Fe deposition, while substantial, were likely not the sole factor in forming the 2022 bloom. This pulse event may have played a considerable role in conjunction with other environmental conditions to stimulate the bloom. Phosphorus availability, horizontal supply of nutrients from higher latitudes, vertical mixing, grazing, and dilution rates likely acted in concert with the elevated Fe supply to create an environment that was favorable for the growth of organisms to form the 2022 bloom. While our data show that the 2022 bloom waters were enriched in Fe and that the bloom waters had received an unusually large pulse of soluble

Fe deposition approximately one month before the bloom initiation, we cannot be certain that Fe deposition alone was responsible for creating the bloom.

4.3. The 2022 Bloom's Impact to the Fe Distributions Below the Surface

Aside from elevated dFe concentrations in the euphotic zone (0–75 m), dFe concentrations observed during the 2022 bloom were broadly consistent with previous summertime observations at or near Station ALOHA (Boyle et al., 2005; Bundy et al., 2025; Fitzsimmons et al., 2015; Hawco et al., 2021, 2022). The dFe minimum in the 2022 Bloom occurred near 125 m (Figure 4a), which typically coincides with the DCM and the 1% photosynthetically active radiation (PAR) depth at Station ALOHA (Rii et al., 2016). However, during the 2022 bloom, both the DCM and the 1% PAR depth shoaled to shallower depths (∼60 and ∼70 m, respectively) due to increased light attenuation associated with the bloom itself (Foreman et al., 2025).

Despite shoaling of the DCM, Fe concentrations remained elevated throughout the upper 75 m, and diatoms and DDA were abundant near the DCM. *Prochlorococcus*, which is typically dominant under Fe-limited conditions, was not abundant within the 2022 bloom; aerosol-derived Fe inputs alleviated Fe limitation in this compressed euphotic zone and was sufficient to support larger, less Fe-efficient taxa (Foreman et al., 2025; Hawco et al., 2020; Sunda & Huntsman, 2015). Thus, while there was a shallower DCM and higher light attenuation in the bloom, the depth of the Fe minima remained similar to what is expected in non-bloom conditions and confirmed the slow vertical mixing in that layer.

Below the dFe minimum, siderophore-mediated activity significantly influences Fe concentrations in the mesopelagic in the NPSG (Bundy et al., 2018). Suspended pFe concentrations increased between 100 and 250 m and were isotopically heavier than dFe, which may indicate an increase in heterotrophic activity and remineralization of light Fe to the dissolved pool near the dFe minimum (Figures 4b, 4d, and 4f). This peak in suspended pFe concentration and δ^{56}pFe results from multiple overlapping processes. These include remineralization of labile, isotopically lighter Fe that leaves behind refractory, isotopically heavier pFe, scavenging of isotopically heavier dFe onto particles, and siderophore-mediated cellular uptake of isotopically heavier, refractory Fe (Ellwood et al., 2015; John et al., 2024; Manck et al., 2022, 2024). Enhanced Fe supply reaching the mesopelagic during the 2022 bloom reduced Fe stress among organisms in this region (Figure 4c), which is corroborated by siderophore uptake studies conducted with water samples from the 2022 bloom (Li et al., 2025). Elevated bioavailable Fe in the 2022 bloom presumably benefitted bacteria in the mesopelagic region, demonstrating microbial sensitivity to episodic aerosol-derived Fe inputs in the NPSG (Li et al., 2025).

The cycling of Fe in the NPSG involves extensive and dynamic processes that occur throughout the water column (Hawco et al., 2022). Fractionation of dFe during organically mediated dust dissolution and recycling of Fe in the oceans results in Fe exchanges between dissolved and particulate pools while maintaining overall mass balance (Boyd et al., 2010, 2017; Conway & John, 2014; John & Adkins, 2012). Supply of Fe from aerosol deposition events preceding the 2022 bloom alleviated Fe stress across both euphotic and mesopelagic zones, highlighting the significant role aerosol inputs play in modulating Fe cycling in the NPSG's ecosystems.

5. Conclusions

Summer phytoplankton blooms in the central NPSG are nearly annual occurrences in a region that is typically depleted in nutrients (Brzezinski et al., 2011; Dore et al., 2008; Follett, Dutkiewicz, et al., 2018; Karl et al., 1992, 2002; C. Wilson et al., 2008). Although these phenomena have been studied for decades, the drivers and mechanisms for the formation and the continuation of these events are not well understood. Thus, it remains difficult to predict their precise location and timing. The 2022 bloom was a large, long-lived phenomenon where the DDA *Hemiaulus hauckii* and *Richelia intercellularis* thrived in the waters of the central NPSG (Foreman et al., 2025). Input of limiting nutrients for diazotrophy, particularly Fe, may have contributed to the bloom's initiation. Observations of dissolved, suspended particulate, and sinking particulate metals within the 2022 bloom indicate higher than usual aerosol Fe deposition preceding the bloom. Our modeling of water parcel back-trajectories combined with modeling of soluble Fe deposition indicate that a particularly large Fe deposition event occurred between 17 and 23 June roughly one month ($t_{\text{-4 weeks}}$) before the formation of the bloom. This 1-month lag observed in our study suggests that physical factors preserved the Fe deposition feature long enough in surface waters for diazotrophs to respond to the elevated Fe concentrations. Our analysis cannot definitively determine whether the $t_{\text{-4 weeks}}$ soluble Fe deposition event played a role in the subsequent 2022 bloom; however,

the methods developed here combining water parcel back trajectory and aerosol deposition models is a useful approach for exploring the role of Fe in stimulating marine phytoplankton productivity.

Conflict of Interest

The authors declare no conflicts of interest relevant to this study.

Data Availability Statement

This study has been conducted using satellite chlorophyll-a data from the E.U. Copernicus Marine Service Information (CMEMS, 2025). Fe and Al data from the PARAGON 2 cruise are available on Zenodo (Kong et al., 2025). Model outputs from our reanalyzes are also available on Zenodo (Kong et al., 2024).

Acknowledgments
The authors would like to thank Tim Burrell, Ryan Tabata, Brandon Brenes, David Karl, Angelique White, Matthew Church, Lauren Manck, Jingxuan Li, Miranda Seixas, and Jennifer Beatty for their support and assistance throughout the PARAGON 2 cruise on the *R/V Kilo Moana* (KM2209). We also thank Emily Seelen, Kiefer Forsch, Jordan Landers, Xiaopeng Bian, and Rachel Kelly for constructive comments and suggestions during revision of this manuscript. This project was funded by the Simons Foundation (Simons Collaboration on Processes and Ecology [SCOPE]; Grants 426570SP and LI-SIAME-00001532 to SGJ), the Simons Foundation International (Grant 9841 to BB), and NASA (Grant 80NSSC24K0446 to DSH). The authors acknowledge the Center for Advanced Research Computing (CARC) at the University of Southern California for providing computing resources that have contributed to the research results reported in this publication. URL: https://carc.usc.edu.

References

Achilles, K. M., Church, T. M., Wilhelm, S. W., Luther, G. I. I. I. W., & Hutchins, D. A. (2003). Bioavailability of iron to Trichodesmium colonies in the western subtropical Atlantic Ocean. *Limnology & Oceanography*, *48*(6), 2250–2255. https://doi.org/10.4319/lo.2003.48.6.2250

Amin, S. A., Green, D. H., Hart, M. C., Küpper, F. C., Sunda, W. G., & Carrano, C. J. (2009). Photolysis of iron–siderophore chelates promotes bacterial–algal mutualism. *Proceedings of the National Academy of Sciences*, *106*(40), 17071–17076. https://doi.org/10.1073/pnas.0905512106

Anderson, E. E., Wilson, C., Knap, A. H., & Villareal, T. A. (2018). Summer diatom blooms in the eastern North Pacific gyre investigated with a long-endurance autonomous surface vehicle. *PeerJ*, *6*, e5387. https://doi.org/10.7717/peerj.5387

Baker, A. R., & Jickells, T. D. (2006). Mineral particle size as a control on aerosol iron solubility. *Geophysical Research Letters*, *33*(17), L07602. https://doi.org/10.1029/2006gl026557

Basu, S., Gledhill, M., Beer, D. D., Matondkar, S. G. P., & Shaked, Y. (2019). Colonies of marine Cyanobacteria Trichodesmium interact with associated bacteria to acquire iron from dust. *Communications Biology*, *2*(1), 284. https://doi.org/10.1038/s42003-019-0534-z

Bates, E. S., & Hawco, N. J. (2025). Dissolved iron seasonal cycle and residence time in the North Pacific Subtropical Gyre. *Geophysical Research Letters*, *52*(21), e2025GL118095. https://doi.org/10.1029/2025GL118095

Bates, E. S., White, A. E., & Hawco, N. J. (2025). Variability and export timescales of upper ocean particulate trace metals in the North Pacific subtropical gyre. *Global Biogeochemical Cycles*, *39*(9), e2025GB008657. https://doi.org/10.1029/2025GB008657

Bathen, K. H. (1972). On the seasonal changes in the depth of the mixed layer in the North Pacific Ocean. *Journal of Geophysical Research*, *77*(36), 7138–7150. https://doi.org/10.1029/jc077i036p07138

Bergas-Masso, E., Hamilton, D. S., Myriokefalitakis, S., Rathod, S., Ageitos, M. G., & García-Pando, C. P. (2025). Future climate-driven fires may boost ocean productivity in the iron-limited North Atlantic. *Nature Climate Change*, *15*(7), 1–9. https://doi.org/10.1038/s41558-025-02356-4

Bonjean, F., & Lagerloef, G. S. E. (2002). Diagnostic model and analysis of the surface currents in the tropical Pacific Ocean. *Journal of Physical Oceanography*, *32*(10), 2938–2954. https://doi.org/10.1175/1520-0485(2002)032<2938:dmaaot>2.0.co;2

Böttjer, D., Dore, J. E., Karl, D. M., Letelier, R. M., Mahaffey, C., Wilson, S. T., et al. (2017). Temporal variability of nitrogen fixation and particulate nitrogen export at Station ALOHA. *Limnology & Oceanography*, *62*(1), 200–216. https://doi.org/10.1002/lno.10386

Boyd, P. W., Ellwood, M. J., Tagliabue, A., & Twining, B. S. (2017). Biotic and abiotic retention, recycling and remineralization of metals in the ocean. *Nature Geoscience*, *10*(3), 167–173. https://doi.org/10.1038/ngeo2876

Boyd, P. W., Mackie, D. S., & Hunter, K. A. (2010). Aerosol iron deposition to the surface ocean—Modes of iron supply and biological responses. *Marine Chemistry*, *120*(1–4), 128–143. https://doi.org/10.1016/j.marchem.2009.01.008

Boyle, E. A., Bergquist, B. A., Kayser, R. A., & Mahowald, N. (2005). Iron, manganese, and lead at Hawaii Ocean Time-series station ALOHA: Temporal variability and an intermediate water hydrothermal plume. *Geochimica et Cosmochimica Acta*, *69*(4), 933–952. https://doi.org/10.1016/j.gca.2004.07.034

Brown, M. T., Landing, W. M., & Measures, C. I. (2005). Dissolved and particulate Fe in the western and central North Pacific: Results from the 2002 IOC cruise. *Geochemistry, Geophysics, Geosystems*, *6*(10), Q10001. https://doi.org/10.1029/2004gc000893

Bruland, K. W., Orians, K. J., & Cowen, J. P. (1994). Reactive trace metals in the stratified central North Pacific. *Geochimica et Cosmochimica Acta*, *58*(15), 3171–3182. https://doi.org/10.1016/0016-7037(94)90044-2

Brzezinski, M., Krause, J. W., Church, M. J., Karl, D. M., Li, B., Jones, J. L., & Updyke, B. (2011). The annual silica cycle of the North Pacific subtropical gyre. *Deep Sea Research Part I: Oceanographic Research Papers*, *58*(10), 988–1001. https://doi.org/10.1016/j.dsr.2011.08.001

Brzezinski, M., Villareal, T., & Lipschultz, F. (1998). Silica production and the contribution of diatoms to new and primary production in the central North Pacific. *Marine Ecology Progress Series*, *167*, 89–104. https://doi.org/10.3354/meps167089

Buck, C. S., Landing, W. M., & Resing, J. (2013). Pacific Ocean aerosols: Deposition and solubility of iron, aluminum, and other trace elements. *Marine Chemistry*, *157*, 117–130. https://doi.org/10.1016/j.marchem.2013.09.005

Buck, C. S., Landing, W. M., Resing, J. A., & Lebon, G. T. (2006). Aerosol iron and aluminum solubility in the northwest Pacific Ocean: Results from the 2002 IOC cruise. *Geochemistry, Geophysics, Geosystems*, *7*(4), Q04M07. https://doi.org/10.1029/2005gc000977

Bundy, R. M., Boiteau, R. M., McLean, C., Turk-Kubo, K. A., McIlvin, M. R., Saito, M. A., et al. (2018). Distinct siderophores contribute to iron cycling in the mesopelagic at station ALOHA. *Frontiers in Marine Science*, *5*, 61. https://doi.org/10.3389/fmars.2018.00061

Bundy, R. M., Manck, L. E., Repeta, D. J., Church, M. J., Hawco, N. J., Boiteau, R. M., et al. (2025). Patterns of siderophore production and utilization at Station ALOHA from the surface to mesopelagic waters. *Limnology & Oceanography*, *70*(1), 128–145. https://doi.org/10.1002/lno.12746

Bunnell, Z. B., Sieber, M., Hamilton, D. S., Marsay, C. M., Buck, C. S., Landing, W. M., et al. (2025). The influence of natural, anthropogenic, and wildfire sources on iron and zinc aerosols delivered to the North Pacific Ocean. *Geophysical Research Letters*, *52*(3), e2024GL113877. https://doi.org/10.1029/2024gl113877

Calil, P. H. R., Doney, S. C., Yumimoto, K., Eguchi, K., & Takemura, T. (2011). Episodic upwelling and dust deposition as bloom triggers in low-nutrient, low-chlorophyll regions. *Journal of Geophysical Research*, *116*(C6), C06030. https://doi.org/10.1029/2010jc006704

Chappell, P. D., Moffett, J. W., Hynes, A. M., & Webb, E. A. (2012). Molecular evidence of iron limitation and availability in the global diazotroph Trichodesmium. *The ISME Journal*, *6*(9), 1728–1739. https://doi.org/10.1038/ismej.2012.13

Chow, C. H., Cheah, W., Letelier, R. M., Karl, D. M., & Tai, J.-H. (2025). Kīlauea Volcanic Ash induced a massive phytoplankton bloom in the nutrient-poor North Pacific subtropical gyre. *Journal of Geophysical Research: Oceans*, *130*(3), e2023JC020676. https://doi.org/10.1029/2023jc020676

Chuang, P. Y., Duvall, R. M., Shafer, M. M., & Schauer, J. J. (2005). The origin of water soluble particulate iron in the Asian atmospheric outflow. *Geophysical Research Letters*, *32*(7), L07813. https://doi.org/10.1029/2004gl021946

Church, M. J., Mahaffey, C., Letelier, R. M., Lukas, R., Zehr, J. P., & Karl, D. M. (2009). Physical forcing of nitrogen fixation and diazotroph community structure in the North Pacific subtropical gyre. *Global Biogeochemical Cycles*, *23*(2), GB2020. https://doi.org/10.1029/2008gb003418

CMEMS. (2025). Global Ocean colour (Copernicus-GlobColour) [Dataset]. *Copernicus Marine Environment Monitoring Service*. https://doi.org/10.48670/moi-00281

Conway, T. M., Hamilton, D. S., Shelley, R. U., Aguilar-Islas, A. M., Landing, W. M., Mahowald, N. M., & John, S. G. (2019). Tracing and constraining anthropogenic aerosol iron fluxes to the North Atlantic Ocean using iron isotopes. *Nature Communications*, *10*(1), 2628. https://doi.org/10.1038/s41467-019-10457-w

Conway, T. M., & John, S. G. (2014). Quantification of dissolved iron sources to the North Atlantic Ocean. *Nature*, *511*(7508), 212–215. https://doi.org/10.1038/nature13482

Conway, T. M., John, S. G., & Sieber, M. (2022). Dissolved concentrations and stable isotope ratios of Fe, Zn, and Cd from Leg 1 (Seattle, WA to Hilo, HI) of the US GEOTRACES Pacific Meridional Transect (PMT) cruise (GP15, RR1814) on R/V Roger Revelle from September to October 2018 [Dataset]. *Biological and Chemical Oceanography Data Management Office (BCO-DMO)*. https://doi.org/10.26008/1912/bco-dmo.883862.1

Conway, T. M., Rosenberg, A. D., Adkins, J. F., & John, S. G. (2013). A new method for precise determination of iron, zinc and cadmium stable isotope ratios in seawater by double-spike mass spectrometry. *Analytica Chimica Acta*, *793*, 44–52. https://doi.org/10.1016/j.aca.2013.07.025

Dai, M., Luo, Y., Achterberg, E. P., Browning, T. J., Cai, Y., Cao, Z., et al. (2023). Upper Ocean biogeochemistry of the oligotrophic North Pacific subtropical gyre: From nutrient sources to carbon export. *Reviews of Geophysics*, *61*(3), e2022RG000800. https://doi.org/10.1029/2022rg000800

Darmenov, A. S., & Silva, A. M. D. (2015). *The Quick Fire Emissions Dataset (QFED): Documentation of Versions 2.1, 2.2 and 2.4 (no. 20180005253)*. National Aeronautics and Space Administration. Retrieved from https://ntrs.nasa.gov/citations/20180005253

Dave, A. C., & Lozier, M. S. (2010). Local stratification control of marine productivity in the subtropical North Pacific. *Journal of Geophysical Research*, *115*(C12), C12032. https://doi.org/10.1029/2010jc006507

DiTullio, G. R., & Laws, E. A. (1991). Impact of an atmospheric-oceanic disturbance on phytoplankton community dynamics in the North Pacific Central Gyre. *Deep-Sea Research, Part A: Oceanographic Research Papers*, *38*(10), 1305–1329. https://doi.org/10.1016/0198-0149(91)90029-f

Dore, J. E., Letelier, R. M., Church, M. J., Lukas, R., & Karl, D. M. (2008). Summer phytoplankton blooms in the oligotrophic North Pacific Subtropical Gyre: Historical perspective and recent observations. *Progress in Oceanography*, *76*(1), 2–38. https://doi.org/10.1016/j.pocean.2007.10.002

Duce, R. A., & Tindale, N. W. (1991). Atmospheric transport of iron and its deposition in the ocean. *Limnology & Oceanography*, *36*(8), 1715–1726. https://doi.org/10.4319/lo.1991.36.8.1715

Ellwood, M. J., Hutchins, D. A., Lohan, M. C., Milne, A., Nasemann, P., Nodder, S. D., et al. (2015). Iron stable isotopes track pelagic iron cycling during a subtropical phytoplankton bloom. *Proceedings of the National Academy of Sciences*, *112*(1), E15–E20. https://doi.org/10.1073/pnas.1421576112

Falkowski, P. G. (1997). Evolution of the nitrogen cycle and its influence on the biological sequestration of CO_2 in the ocean. *Nature*, *387*(6630), 272–275. https://doi.org/10.1038/387272a0

Falkowski, P. G., Barber, R. T., & Smetacek, V. (1998). Biogeochemical controls and feedbacks on Ocean primary production. *Science*, *281*(5374), 200–206. https://doi.org/10.1126/science.281.5374.200

Field, C. B., Behrenfeld, M. J., Randerson, J. T., & Falkowski, P. (1998). Primary production of the biosphere: Integrating terrestrial and Oceanic components. *Science*, *281*(5374), 237–240. https://doi.org/10.1126/science.281.5374.237

Fitzsimmons, J. N., & Conway, T. M. (2022). Novel insights into Marine iron biogeochemistry from iron isotopes. *Annual Review of Marine Science*, *15*(1), 383–406. https://doi.org/10.1146/annurev-marine-032822-103431

Fitzsimmons, J. N., Hayes, C. T., Al-Subiai, S. N., Zhang, R., Morton, P. L., Weisend, R. E., et al. (2015). Daily to decadal variability of size-fractionated iron and iron-binding ligands at the Hawaii Ocean Time-series Station ALOHA. *Geochimica et Cosmochimica Acta*, *171*, 303–324. https://doi.org/10.1016/j.gca.2015.08.012

Follett, C. L., Dutkiewicz, S., Karl, D. M., Inomura, K., & Follows, M. J. (2018). Seasonal resource conditions favor a summertime increase in North Pacific diatom–diazotroph associations. *The ISME Journal*, *12*(6), 1543–1557. https://doi.org/10.1038/s41396-017-0012-x

Follett, C. L., White, A. E., Wilson, S. T., & Follows, M. J. (2018). Nitrogen fixation rates diagnosed from diurnal changes in elemental stoichiometry. *Limnology & Oceanography*, *63*(5), 1911–1923. https://doi.org/10.1002/lno.10815

Fong, A. A., Karl, D. M., Lukas, R., Letelier, R. M., Zehr, J. P., & Church, M. J. (2008). Nitrogen fixation in an anticyclonic eddy in the oligotrophic North Pacific Ocean. *The ISME Journal*, *2*(6), 663–676. https://doi.org/10.1038/ismej.2008.22

Foreman, R. K., Barone, B., Grabowski, E., Björkman, K. M., Freitas, F. H., Garcia, C., et al. (2025). Biogeochemical anatomy and ecosystem dynamics of a large phytoplankton bloom north of the Hawaiian Islands. *Progress in Oceanography*, *241*, 103620. https://doi.org/10.1016/j.pocean.2025.103620

Grabowski, M., Church, M., & Karl, D. (2008). Nitrogen fixation rates and controls at Stn ALOHA. *Aquatic Microbial Ecology*, *52*, 175–183. https://doi.org/10.3354/ame01209

Guieu, C., Bonnet, S., Wagener, T., & Loÿe-Pilot, M. (2005). Biomass burning as a source of dissolved iron to the open ocean? *Geophysical Research Letters*, *32*(19), L19608. https://doi.org/10.1029/2005gl022962

Hamilton, D. S., Scanza, R. A., Feng, Y., Guinness, J., Kok, J. F., Li, L., et al. (2019). Improved methodologies for Earth system modelling of atmospheric soluble iron and observation comparisons using the Mechanism of Intermediate complexity for Modelling Iron (MIMI v1.0). *Geoscientific Model Development*, *12*(9), 3835–3862. https://doi.org/10.5194/gmd-12-3835-2019

Hamilton, D. S., Scanza, R. A., Rathod, S. D., Bond, T. C., Kok, J. F., Li, L., et al. (2020). Recent (1980 to 2015) trends and variability in daily-to-interannual soluble iron deposition from dust, fire, and anthropogenic sources. *Geophysical Research Letters*, *47*(17), e2020GL089688. https://doi.org/10.1029/2020gl089688

Harke, M. J., Frischkorn, K. R., Haley, S. T., Aylward, F. O., Zehr, J. P., & Dyhrman, S. T. (2019). Periodic and coordinated gene expression between a diazotroph and its diatom host. *The ISME Journal*, *13*(1), 118–131. https://doi.org/10.1038/s41396-018-0262-2

Hawco, N. J., Barone, B., Church, M. J., Babcock-Adams, L., Repeta, D. J., Wear, E. K., et al. (2021). Iron depletion in the deep chlorophyll maximum: Mesoscale eddies as natural iron fertilization experiments. *Global Biogeochemical Cycles*, *35*(12), e2021GB007112. https://doi.org/10.1029/2021gb007112

Hawco, N. J., Conway, T. M., Coesel, S. N., Barone, B., Seelen, E. A., Yang, S.-C., et al. (2025). Anthropogenic iron alters the spring phytoplankton bloom in the North Pacific transition zone. *Proceedings of the National Academy of Sciences of the United States of America*, *122*(23), e2418201122. https://doi.org/10.1073/pnas.2418201122

Hawco, N. J., Fu, F., Yang, N., Hutchins, D. A., & John, S. G. (2020). Independent iron and light limitation in a low-light-adapted Prochlorococcus from the deep chlorophyll maximum. *The ISME Journal*, *15*(1), 359–362. https://doi.org/10.1038/s41396-020-00776-y

Hawco, N. J., Yang, S., Pinedo-González, P., Black, E. E., Kenyon, J., Ferrón, S., et al. (2022). Recycling of dissolved iron in the North Pacific Subtropical Gyre. *Limnology & Oceanography*, *67*(11), 2448–2465. https://doi.org/10.1002/lno.12212

Huffman, G. J., Stocker, E. F., Bolvin, D. T., Nelkin, E. J., & Tan, J. (2019). GPM IMERG Late Precipitation L3 1 day 0.1 degree x 0.1 degree V06. Retrieved October 10, 2024, from Goddard Earth Sciences Data and Information Services Center (GES DISC). https://doi.org/10.5067/GPM/IMERGDL/DAY/07

Hutchins, D. A., & Sañudo-Wilhelmy, S. A. (2021). The enzymology of Ocean global change. *Annual Review of Marine Science*, *14*(1), 1–25. https://doi.org/10.1146/annurev-marine-032221-084230

Iida, Y., Takatani, Y., Kojima, A., & Ishii, M. (2021). Global trends of ocean CO_2 sink and ocean acidification: An observation-based reconstruction of surface ocean inorganic carbon variables. *Journal of Oceanography*, *77*(2), 323–358. https://doi.org/10.1007/s10872-020-00571-5

Ingalls, A. E., Anderson, R. F., & Pearson, A. (2004). Radiocarbon dating of diatom-bound organic compounds. *Marine Chemistry*, *92*(1–4), 91–105. https://doi.org/10.1016/j.marchem.2004.06.019

Ito, A., Myriokefalitakis, S., Kanakidou, M., Mahowald, N. M., Scanza, R. A., Hamilton, D. S., et al. (2019). Pyrogenic iron: The missing link to high iron solubility in aerosols. *Science Advances*, *5*(5), eaau7671. https://doi.org/10.1126/sciadv.aau7671

Jacq, V., Ridame, C., L'Helguen, S., Kaczmar, F., & Saliot, A. (2014). Response of the unicellular diazotrophic cyanobacterium Crocosphaera watsonii to iron limitation. *PLoS One*, *9*(1), e86749. https://doi.org/10.1371/journal.pone.0086749

Jiang, H.-B., Fu, F.-X., Rivero-Calle, S., Levine, N. M., Sañudo-Wilhelmy, S. A., Qu, P.-P., et al. (2018). Ocean warming alleviates iron limitation of marine nitrogen fixation. *Nature Climate Change*, *8*(8), 709–712. https://doi.org/10.1038/s41558-018-0216-8

Jickells, T. D., An, Z. S., Andersen, K. K., Baker, A. R., Bergametti, G., Brooks, N., et al. (2005). Global Iron connections between desert dust, Ocean Biogeochemistry, and climate. *Science*, *308*(5718), 67–71. https://doi.org/10.1126/science.1105959

John, S. G., & Adkins, J. (2012). The vertical distribution of iron stable isotopes in the North Atlantic near Bermuda. *Global Biogeochemical Cycles*, *26*(2), GB2034. https://doi.org/10.1029/2011gb004043

John, S. G., Boyle, E. A., Cunningham, B. R., Fu, F.-X., Greene, S., Hodierne, C., et al. (2024). Kinetic isotope effects during reduction of Fe(III) to Fe(II): Large normal and inverse isotope effects for abiotic reduction and smaller fractionations by phytoplankton in culture. *Geochemistry, Geophysics, Geosystems*, *25*(6), e2023GC010952. https://doi.org/10.1029/2023gc010952

Karl, D. M. (1999). A Sea of change: Biogeochemical variability in the North Pacific subtropical gyre. *Ecosystems*, *2*(3), 181–214. https://doi.org/10.1007/s100219900068

Karl, D. M. (2002). Nutrient dynamics in the deep blue sea. *Trends in Microbiology*, *10*(9), 410–418. https://doi.org/10.1016/s0966-842x(02)02430-7

Karl, D. M., Church, M. J., Dore, J. E., Letelier, R. M., & Mahaffey, C. (2012). Predictable and efficient carbon sequestration in the North Pacific Ocean supported by symbiotic nitrogen fixation. *Proceedings of the National Academy of Sciences*, *109*(6), 1842–1849. https://doi.org/10.1073/pnas.1120312109

Karl, D. M., Letelier, R., Hebel, D. V., Bird, D. F., & Winn, C. D. (1992). Marine pelagic cyanobacteria: Trichodesmium and other diazotrophs (pp. 219–237). https://doi.org/10.1007/978-94-015-7977-3_14

Karl, D. M., Letelier, R., Tupas, L., Dore, J., Christian, J., & Hebel, D. (1997). The role of nitrogen fixation in biogeochemical cycling in the subtropical North Pacific Ocean. *Nature*, *388*(6642), 533–538. https://doi.org/10.1038/41474

Karl, D. M., Letelier, R. M., Bidigare, R. R., Björkman, K. M., Church, M. J., Dore, J. E., & White, A. E. (2021). Seasonal-to-decadal scale variability in primary production and particulate matter export at Station ALOHA. *Progress in Oceanography*, *195*, 102563. https://doi.org/10.1016/j.pocean.2021.102563

Karl, D. M., Michaels, A., Bergman, B., Capone, D., Carpenter, E., Letelier, R., et al. (2002). The nitrogen cycle at regional to global scales. In *The nitrogen cycle at regional to global scales* (pp. 47–98). https://doi.org/10.1007/978-94-017-3405-9_2

Knauer, G. A., Martin, J. H., & Bruland, K. W. (1979). Fluxes of particulate carbon, nitrogen, and phosphorus in the upper water column of the northeast Pacific. *Deep-Sea Research, Part A: Oceanographic Research Papers*, *26*(1), 97–108. https://doi.org/10.1016/0198-0149(79)90089-x

Kok, J. F. (2011). A scaling theory for the size distribution of emitted dust aerosols suggests climate models underestimate the size of the global dust cycle. *Proceedings of the National Academy of Sciences*, *108*(3), 1016–1021. https://doi.org/10.1073/pnas.1014798108

Kok, J. F., Adebiyi, A. A., Albani, S., Balkanski, Y., Checa-Garcia, R., Chin, M., et al. (2021). Contribution of the world's main dust source regions to the global cycle of desert dust. *Atmospheric Chemistry and Physics*, *21*(10), 8169–8193. https://doi.org/10.5194/acp-21-8169-2021

Kok, J. F., Mahowald, N. M., Fratini, G., Gillies, J. A., Ishizuka, M., Leys, J. F., et al. (2014). An improved dust emission model—Part 1: Model description and comparison against measurements. *Atmospheric Chemistry and Physics*, *14*(23), 13023–13041. https://doi.org/10.5194/acp-14-13023-2014

Kok, J. F., Ridley, D. A., Zhou, Q., Miller, R. L., Zhao, C., Heald, C. L., et al. (2017). Smaller desert dust cooling effect estimated from analysis of dust size and abundance. *Nature Geoscience*, *10*(4), 274–278. https://doi.org/10.1038/ngeo2912

Kong, K., John, S. G., Barone, B., & Hamilton, D. S. (2024). Modeled Fe deposition fluxes and Chl from 2022 Bloom back trajectories in the NPSG [Dataset]. *Zenodo*. https://doi.org/10.5281/zenodo.14574643

Kong, K., Yang, S. C., & John, S. G. (2025). Paragon 2—KM2209—Trace metals data [Dataset]. *Zenodo*. https://doi.org/10.5281/zenodo.17857911

Kranzler, C., Kessler, N., Keren, N., & Shaked, Y. (2016). Enhanced ferrihydrite dissolution by a unicellular, planktonic cyanobacterium: A biological contribution to particulate iron bioavailability. *Environmental Microbiology*, *18*(12), 5101–5111. https://doi.org/10.1111/1462-2920.13496

Kurisu, M., Adachi, K., Sakata, K., & Takahashi, Y. (2019). Stable isotope ratios of combustion iron produced by evaporation in a steel plant. *ACS Earth and Space Chemistry*, *3*(4), 588–598. https://doi.org/10.1021/acsearthspacechem.8b00171

Kurisu, M., Sakata, K., Uematsu, M., Ito, A., & Takahashi, Y. (2021). Contribution of combustion Fe in marine aerosols over the northwestern Pacific estimated by Fe stable isotope ratios. *Atmospheric Chemistry and Physics*, *21*(20), 16027–16050. https://doi.org/10.5194/acp-21-16027-2021

Lagerström, M. E., Field, M. P., Séguret, M., Fischer, L., Hann, S., & Sherrell, R. M. (2013). Automated on-line flow-injection ICP-MS determination of trace metals (Mn, Fe, Co, Ni, Cu and Zn) in open ocean seawater: Application to the GEOTRACES program. *Marine Chemistry*, *155*, 71–80. https://doi.org/10.1016/j.marchem.2013.06.001

Lam, P. J., Lee, J.-M., Amaral, V. J., Laubach, A., Carracino, N., Rojas, S., & Mateos, K. (2024). Size-fractionated major, minor, & trace particle composition and concentration from Leg 1 (Seattle, WA to Hilo, HI) of the US GEOTRACES Pacific Meridional Transect (PMT) cruise (GP15, RR1814) on R/V Roger Revelle from Sept to Oct 2018 (Version 1) [Dataset]. *Biological and Chemical Oceanography Data Management Office (BCO-DMO)*. https://doi.org/10.26008/1912/bco-dmo.918811.1

Lam, P. J., Lee, J.-M., Heller, M. I., Mehic, S., Xiang, Y., & Bates, N. R. (2018). Size-fractionated distributions of suspended particle concentration and major phase composition from the U.S. GEOTRACES Eastern Pacific Zonal Transect (GP16). *Marine Chemistry*, *201*, 90–107. https://doi.org/10.1016/j.marchem.2017.08.013

Lamborg, C. H., Buesseler, K. O., & Lam, P. J. (2008). Sinking fluxes of minor and trace elements in the North Pacific Ocean measured during the VERTIGO program. *Deep Sea Research Part II: Topical Studies in Oceanography*, *55*(14–15), 1564–1577. https://doi.org/10.1016/j.dsr2.2008.04.012

Letelier, R. M., Björkman, K. M., Church, M. J., Hamilton, D. S., Mahowald, N. M., Scanza, R. A., et al. (2019). Climate-driven oscillation of phosphorus and iron limitation in the North Pacific Subtropical Gyre. *Proceedings of the National Academy of Sciences*, *116*(26), 12720–12728. https://doi.org/10.1073/pnas.1900789116

Li, J., Babcock-Adams, L., McIlvin, M. R., & Repeta, D. J. (2025). Distribution and cycling of siderophores in the Eastern north and tropical Pacific Oceans. *Geophysical Research Letters*, *52*(6), e2024GL113874. https://doi.org/10.1029/2024gl113874

Mague, T. H., Weare, N. M., & Holm-Hansen, O. (1974). Nitrogen fixation in the North Pacific Ocean. *Marine Biology*, *24*(2), 109–119. https://doi.org/10.1007/bf00389344

Mahowald, N. M., Baker, A. R., Bergametti, G., Brooks, N., Duce, R. A., Jickells, T. D., et al. (2005). Atmospheric global dust cycle and iron inputs to the ocean. *Global Biogeochemical Cycles*, *19*(4), GB4025. https://doi.org/10.1029/2004gb002402

Malm, W. C., Sisler, J. F., Huffman, D., Eldred, R. A., & Cahill, T. A. (1994). Spatial and seasonal trends in particle concentration and optical extinction in the United States. *Journal of Geophysical Research*, *99*(D1), 1347–1370. https://doi.org/10.1029/93jd02916

Manck, L. E., Coale, T. H., Stephens, B. M., Forsch, K. O., Aluwihare, L. I., Dupont, C. L., et al. (2024). Iron limitation of heterotrophic bacteria in the California Current System tracks relative availability of organic carbon and iron. *The ISME Journal*, *18*(1), wrae061. https://doi.org/10.1093/ismejo/wrae061

Manck, L. E., Park, J., Tully, B. J., Poire, A. M., Bundy, R. M., Dupont, C. L., & Barbeau, K. A. (2022). Petrobactin, a siderophore produced by Alteromonas, mediates community iron acquisition in the global ocean. *The ISME Journal*, *16*(2), 358–369. https://doi.org/10.1038/s41396-021-01065-y

Marsay, C. M., Kadko, D., Landing, W. M., & Buck, C. S. (2022). Bulk aerosol trace element concentrations and deposition fluxes during the U.S. GEOTRACES GP15 Pacific meridional transect. *Global Biogeochemical Cycles*, *36*(2), e2021GB007122. https://doi.org/10.1029/2021gb007122

Martin, J. H., & Fitzwater, S. E. (1988). Iron deficiency limits phytoplankton growth in the north-east Pacific subarctic. *Nature*, *331*(6154), 341–343. https://doi.org/10.1038/331341a0

McLennan, S. M. (2001). Relationships between the trace element composition of sedimentary rocks and upper continental crust. *Geochemistry, Geophysics, Geosystems*, *2*(4), 1021. https://doi.org/10.1029/2000gc000109

Mead, C., Herckes, P., Majestic, B. J., & Anbar, A. D. (2013). Source apportionment of aerosol iron in the marine environment using iron isotope analysis. *Geophysical Research Letters*, *40*(21), 5722–5727. https://doi.org/10.1002/2013gl057713

Measures, C. I., Sato, T., Vink, S., Howell, S., & Li, Y. H. (2010). The fractional solubility of aluminium from mineral aerosols collected in Hawaii and implications for atmospheric deposition of biogeochemically important trace elements. *Marine Chemistry*, *120*(1–4), 144–153. https://doi.org/10.1016/j.marchem.2009.01.014

Mills, M. M., Ridame, C., Davey, M., Roche, J. L., & Geider, R. J. (2004). Iron and phosphorus co-limit nitrogen fixation in the eastern tropical North Atlantic. *Nature*, *429*(6989), 292–294. https://doi.org/10.1038/nature02550

Moore, C. M., Mills, M. M., Achterberg, E. P., Geider, R. J., LaRoche, J., Lucas, M. I., et al. (2009). Large-scale distribution of Atlantic nitrogen fixation controlled by iron availability. *Nature Geoscience*, *2*(12), 867–871. https://doi.org/10.1038/ngeo667

Noble, A. E., Moran, D. M., Allen, A. E., & Saito, M. A. (2013). Dissolved and particulate trace metal micronutrients under the McMurdo Sound seasonal sea ice: Basal sea ice communities as a capacitor for iron. *Frontiers in Chemistry*, *1*, 25. https://doi.org/10.3389/fchem.2013.00025

Ohnemus, D. C., Kollman, C., Marsay, C. M., Ricci, M., & Buck, C. S. (2025). The Hawaii dust regime: Patterns and variability in aerosol mineral dust from MERRA-2 at station ALOHA and the Hawaii aerosol time-series. *Journal of Geophysical Research: Atmospheres*, *130*(1), e2024JD041860. https://doi.org/10.1029/2024jd041860

Onu, K., Huhn, F., & Haller, G. (2015). LCS tool: A computational platform for Lagrangian coherent structures. *Journal of Computational Science*, *7*, 26–36. https://doi.org/10.1016/j.jocs.2014.12.002

Orians, K. J., & Bruland, K. W. (1986). The biogeochemistry of aluminum in the Pacific Ocean. *Earth and Planetary Science Letters*, *78*(4), 397–410. https://doi.org/10.1016/0012-821x(86)90006-3

Palmer, J. R., & Totterdell, I. J. (2001). Production and export in a global ocean ecosystem model. *Deep Sea Research Part I: Oceanographic Research Papers*, *48*(5), 1169–1198. https://doi.org/10.1016/s0967-0637(00)00080-7

Pinedo-González, P., Hawco, N. J., Bundy, R. M., Armbrust, E. V., Follows, M. J., Cael, B. B., et al. (2020). Anthropogenic Asian aerosols provide Fe to the North Pacific Ocean. *Proceedings of the National Academy of Sciences of the United States of America*, *117*(45), 27862–27868. https://doi.org/10.1073/pnas.2010315117

Planquette, H., & Sherrell, R. M. (2012). Sampling for particulate trace element determination using water sampling bottles: Methodology and comparison to in situ pumps. *Limnology and Oceanography: Methods*, *10*(5), 367–388. https://doi.org/10.4319/lom.2012.10.367

Quay, P., & Stutsman, J. (2003). Surface layer carbon budget for the subtropical N. Pacific: $\delta^{13}C$ constraints at station ALOHA. *Deep Sea Research Part I: Oceanographic Research Papers*, *50*(9), 1045–1061. https://doi.org/10.1016/s0967-0637(03)00116-x

Rathod, S. D., Hamilton, D. S., Mahowald, N. M., Klimont, Z., Corbett, J. J., & Bond, T. C. (2020). A mineralogy-based anthropogenic combustion-iron emission inventory. *Journal of Geophysical Research: Atmospheres*, *125*(17), e2019JD032114. https://doi.org/10.1029/2019jd032114

Rathod, S. D., Hamilton, D. S., Nino, L., Kreidenweis, S. M., Bian, Q., Mahowald, N. M., et al. (2024). Constraining present-day anthropogenic total iron emissions using model and observations. *Journal of Geophysical Research: Atmospheres*, *129*(17), e2023JD040332. https://doi.org/10.1029/2023jd040332

Ridley, D. A., Heald, C. L., Kok, J. F., & Zhao, C. (2016). An observationally constrained estimate of global dust aerosol optical depth. *Atmospheric Chemistry and Physics*, *16*(23), 15097–15117. https://doi.org/10.5194/acp-16-15097-2016

Rii, Y., Karl, D., & Church, M. (2016). Temporal and vertical variability in picophytoplankton primary productivity in the North Pacific Subtropical Gyre. *Marine Ecology Progress Series*, *562*, 1–18. https://doi.org/10.3354/meps11954

Rubin, M., Berman-Frank, I., & Shaked, Y. (2011). Dust- and mineral-iron utilization by the marine dinitrogen-fixer Trichodesmium. *Nature Geoscience*, *4*(8), 529–534. https://doi.org/10.1038/ngeo1181

Rudnick, R. L., & Gao, S. (2014). Treatise on geochemistry (2nd ed., pp. 1–51). https://doi.org/10.1016/b978-0-08-095975-7.00301-6

Scanza, R. A., Mahowald, N., Ghan, S., Zender, C. S., Kok, J. F., Liu, X., et al. (2015). Modeling dust as component minerals in the Community Atmosphere Model: Development of framework and impact on radiative forcing. *Atmospheric Chemistry and Physics*, *15*(1), 537–561. https://doi.org/10.5194/acp-15-537-2015

Schroth, A. W., Crusius, J., Sholkovitz, E. R., & Bostick, B. C. (2009). Iron solubility driven by speciation in dust sources to the ocean. *Nature Geoscience*, *2*(5), 337–340. https://doi.org/10.1038/ngeo501

Sedwick, P. N., Sholkovitz, E. R., & Church, T. M. (2007). Impact of anthropogenic combustion emissions on the fractional solubility of aerosol iron: Evidence from the Sargasso Sea. *Geochemistry, Geophysics, Geosystems*, *8*(10). https://doi.org/10.1029/2007gc001586

Seelen, E. A., Gleich, S. J., Kumler, W., Anderson, H. S., Bian, X., Björkman, K. M., et al. (2025). Nitrogen and phosphorus differentially control marine biomass production and stoichiometry. *Nature Communications*, *16*(1), 5713. https://doi.org/10.1038/s41467-025-61061-0

Sholkovitz, E. R., Sedwick, P. N., & Church, T. M. (2009). Influence of anthropogenic combustion emissions on the deposition of soluble aerosol iron to the ocean: Empirical estimates for island sites in the North Atlantic. *Geochimica et Cosmochimica Acta*, *73*(14), 3981–4003. https://doi.org/10.1016/j.gca.2009.04.029

Siebert, C., Nägler, T. F., & Kramers, J. D. (2001). Determination of molybdenum isotope fractionation by double-spike multicollector inductively coupled plasma mass spectrometry. *Geochemistry, Geophysics, Geosystems*, *2*(7), 16. https://doi.org/10.1029/2000gc000124

Smith, M. B., Mahowald, N. M., Albani, S., Perry, A., Losno, R., Qu, Z., et al. (2017). Sensitivity of the interannual variability of mineral aerosol simulations to meteorological forcing dataset. *Atmospheric Chemistry and Physics*, *17*(5), 3253–3278. https://doi.org/10.5194/acp-17-3253-2017

Sohm, J. A., Subramaniam, A., Gunderson, T. E., Carpenter, E. J., & Capone, D. G. (2011). Nitrogen fixation by Trichodesmium spp. and unicellular diazotrophs in the North Pacific Subtropical Gyre. *Journal of Geophysical Research*, *116*(G3), G03002. https://doi.org/10.1029/2010jg001513

Sohm, J. A., Webb, E. A., & Capone, D. G. (2011). Emerging patterns of marine nitrogen fixation. *Nature Reviews Microbiology*, *9*(7), 499–508. https://doi.org/10.1038/nrmicro2594

Sunda, W. G., & Huntsman, S. A. (2015). High iron requirement for growth, photosynthesis, and low-light acclimation in the coastal cyanobacterium Synechococcus bacillaris. *Frontiers in Microbiology*, *6*, 561. https://doi.org/10.3389/fmicb.2015.00561

Tanita, I., Shiozaki, T., Kodama, T., Hashihama, F., Sato, M., Takahashi, K., & Furuya, K. (2021). Regionally variable responses of nitrogen fixation to iron and phosphorus enrichment in the Pacific Ocean. *Journal of Geophysical Research: Biogeosciences*, *126*(9), e2021JG006542. https://doi.org/10.1029/2021jg006542

Trapp, J. M., Millero, F. J., & Prospero, J. M. (2010). Trends in the solubility of iron in dust-dominated aerosols in the equatorial Atlantic trade winds: Importance of iron speciation and sources. *Geochemistry, Geophysics, Geosystems*, *11*(3). https://doi.org/10.1029/2009gc002651

Twining, B. S., & Baines, S. B. (2013). The trace metal composition of Marine Phytoplankton. *Marine Science*, *5*(1), 191–215. https://doi.org/10.1146/annurev-marine-121211-172322

Villareal, T. A., Adornato, L., Wilson, C., & Schoenbaechler, C. A. (2011). Summer blooms of diatom-diazotroph assemblages and surface chlorophyll in the North Pacific gyre: A disconnect. *Journal of Geophysical Research*, *116*(C3), C03001. https://doi.org/10.1029/2010jc006268

Vitousek, P. M., & Howarth, R. W. (1991). Nitrogen limitation on land and in the sea: How can it occur? *Biogeochemistry*, *13*(2), 87–115. https://doi.org/10.1007/bf00002772

Waite, T. D., & Morel, F. M. M. (1984). Photoreductive dissolution of colloidal iron oxides in natural waters. *Environmental Science & Technology*, *18*(11), 860–868. https://doi.org/10.1021/es00129a010

Webb, E. A., Jakuba, R. W., Moffett, J. W., & Dyhrman, S. T. (2007). Molecular assessment of phosphorus and iron physiology in Trichodesmium populations from the western Central and western South Atlantic. *Limnology & Oceanography*, *52*(5), 2221–2232. https://doi.org/10.4319/lo.2007.52.5.2221

Whittaker, S., Bidle, K. D., Kustka, A. B., & Falkowski, P. G. (2011). Quantification of nitrogenase in Trichodesmium IMS 101: Implications for iron limitation of nitrogen fixation in the ocean. *Environmental Microbiology Reports*, *3*(1), 54–58. https://doi.org/10.1111/j.1758-2229.2010.00187.x

Wiedinmyer, C., Akagi, S. K., Yokelson, R. J., Emmons, L. K., Al-Saadi, J. A., Orlando, J. J., & Soja, A. J. (2011). The Fire INventory from NCAR (FINN): A high resolution global model to estimate the emissions from open burning. *Geoscientific Model Development*, *4*(3), 625–641. https://doi.org/10.5194/gmd-4-625-2011

Wilson, C. (2003). Late summer chlorophyll blooms in the oligotrophic North Pacific Subtropical Gyre. *Geophysical Research Letters*, *30*(18), 1942. https://doi.org/10.1029/2003gl017770

Wilson, C. (2021). Evidence of episodic nitrate injections in the oligotrophic North Pacific associated with surface chlorophyll blooms. *Journal of Geophysical Research: Oceans*, *126*(11), e2021JC017169. https://doi.org/10.1029/2021jc017169

Wilson, C., & Coles, V. J. (2005). Global climatological relationships between satellite biological and physical observations and upper ocean properties. *Journal of Geophysical Research*, *110*(C10), C10001. https://doi.org/10.1029/2004jc002724

Wilson, C., Villareal, T. A., Maximenko, N., Bograd, S. J., Montoya, J. P., & Schoenbaechler, C. A. (2008). Biological and physical forcings of late summer chlorophyll blooms at 30°N in the oligotrophic Pacific. *Journal of Marine Systems*, *69*(3–4), 164–176. https://doi.org/10.1016/j.jmarsys.2005.09.018

Wilson, S. T., Aylward, F. O., Ribalet, F., Barone, B., Casey, J. R., Connell, P. E., et al. (2017). Coordinated regulation of growth, activity and transcription in natural populations of the unicellular nitrogen-fixing cyanobacterium crocosphaera. *Nature Microbiology*, *2*(9), 17118. https://doi.org/10.1038/nmicrobiol.2017.118

Yang, N., Merkel, C. A., Lin, Y.-A., Levine, N. M., Hawco, N. J., Jiang, H.-B., et al. (2021). Warming iron-limited oceans enhance nitrogen fixation and drive biogeographic specialization of the globally important cyanobacterium crocosphaera. *Frontiers in Marine Science*, *8*, 628363. https://doi.org/10.3389/fmars.2021.628363

Zehr, J. P., & Capone, D. G. (2020). Changing perspectives in marine nitrogen fixation. *Science*, *368*(6492), eaay9514. https://doi.org/10.1126/science.aay9514

Zender, C. S., Bian, H., & Newman, D. (2003). Mineral Dust Entrainment and Deposition (DEAD) model: Description and 1990s dust climatology. *Journal of Geophysical Research*, *108*(D14), 4416. https://doi.org/10.1029/2002jd002775

Zhang, T., Liu, J., Xiang, Y., Liu, X., Zhang, J., Zhang, L., et al. (2024). Quantifying anthropogenic emission of iron in marine aerosol in the Northwest Pacific with shipborne online measurements. *Science of the Total Environment*, *912*, 169158. https://doi.org/10.1016/j.scitotenv.2023.169158

References From the Supporting Information

Shelley, R. U., Morton, P. L., & Landing, W. M. (2015). Elemental ratios and enrichment factors in aerosols from the US-GEOTRACES North Atlantic transects. *Deep Sea Research Part II: Topical Studies in Oceanography*, *116*, 262–272. https://doi.org/10.1016/j.dsr2.2014.12.005